

ACOUSTIC IMAGING OF GEOSYNCHRONOUS SATELLITES VIA A NEWLY UPGRADED HYPER-  
TEMPORAL IMAGING INSTRUMENT

By  
Marita D. Morris

---

Copyright © Marita D. Morris 2018

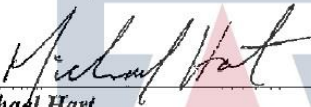
A Thesis Submitted to the Faculty of the  
  
COLLEGE OF OPTICAL SCIENCES

In Partial Fulfillment of the Requirements  
For the Degree of  
  
MASTER OF SCIENCE


In the Graduate College  
  
THE UNIVERSITY OF ARIZONA  
2018

THE UNIVERSITY OF ARIZONA  
GRADUATE COLLEGE

As members of the Master's Committee, we certify that we have read the thesis prepared by *Marita Morris*, titled *Acoustic Imaging of Geosynchronous Satellites via a Newly Upgraded Hyper-Temporal Imaging Instrument* and recommend that it be accepted as fulfilling the thesis requirement for the Master's Degree.

  
\_\_\_\_\_  
Michael Hart

Date: 12/7/18

  
\_\_\_\_\_  
Jose Sasián


Date: 12/7/18

  
\_\_\_\_\_  
Christoph Baranec

Date: 12/7/18

Final approval and acceptance of this thesis is contingent upon the candidate's submission of the final copies of the thesis to the Graduate College.

I hereby certify that I have read this thesis prepared under my direction and recommend that it be accepted as fulfilling the Master's requirement.

  
\_\_\_\_\_  
Michael Hart  
Associate Professor  
Optical Sciences

Date: 12/7/18

## Table of Contents

0 Abstract .....	4
1 The Need for Hyper-Temporal Imaging .....	5
1.1 Sensing and Resolving satellites using conventional methods .....	5
1.2 Polarization and Satellites, Background .....	6
1.3 Previous Implementation of HTI, Version 1 .....	7
2 HTI Upgrade Design .....	11
2.1 The Telescope and Site .....	11
2.2 Optical Design of HTI Upgrade .....	15
2.2.1 Light Path and Lens System .....	15
2.2.2 Detector Specifications (2 Different Configurations: Flir Grasshopper and Andor Zyla) .....	21
3 HTI on the telescope .....	26
3.1 Experimental Design – Aim of the Observations .....	26
3.2 The Satellites .....	28
3.3 First Observations Using the Flir Grasshopper Detectors (May) .....	32
3.4 Second Observations using the Andor Zyla Detectors (July, Aug, Sept, Oct) .....	32
4 Data Analysis .....	34
4.1 Basic Outline .....	34
4.2 Comparison of Several Target Satellites and Stars .....	37
4.2.1 Satellite Ciel-2 [NORAD ID: 33453] .....	37
4.2.2 Satellite StarOne/Brasilsat B4 [NORAD ID: 26469] .....	41
4.2.3 Satellite DirecTV-15 [NORAD ID: 40663] .....	46
4.2.4 Stars as Comparison .....	48
4.3 Comparison of Signal with Telescope Tracking On and Off .....	49
4.4 Noise in the Signal: Clouds vs Signal .....	50
5 Results and Discussion .....	52
5.1 Performance of the HTI Instrument Upgrade .....	52
5.2 Result of Comparison of Several targets (Observational Results) .....	53
5.3 Discussion .....	54
6 Appendices .....	55
6.1 List of Data Figures .....	55
6.2 MATLAB code package definitions .....	71
7 References .....	77

## Abstract

Presented here are investigations into acoustic imaging techniques designed to identify geosynchronous (GEO) satellites by their polarization signatures.

In order to conduct these observations, a hyper-temporal imaging (HTI) instrument has been developed. This new instrument has been designed to operate on the 61" Kuiper telescope, located on Mount Bigelow, Arizona. At the core of HTI is a polarizing beam splitter and two identical cameras which record s and p linear polarized channels simultaneously. These two channels are then used to calculate degree of linear polarization of the signal over time. The latest upgraded cameras are each Andor Zyla 4.2+sCMOS. These cameras are capable of recording data at speeds greater than 1000fps with a Field of View of 5 arcminutes. Typical site conditions at the telescope give an estimated 1 arcsecond of seeing (on good nights), thus the optical aberrations in HTI have been designed to be far less than this limit.

Observations with the HTI instrument were conducted over 10 nights and data were collected on 22 different GEO satellites plus several stars for comparison. Here three of these target satellites are analyzed in detail for their unique signatures. StarOne/Brasilsat B4 (HS-376W bus) is a known spin-stabilized satellite. It showed clear peaks in the signal of: 0.53Hz, 1.06Hz, 1.59Hz, 2.1Hz, 2.65Hz, 3.18Hz, and 3.71Hz. Ciel-2 (Spacebus-4000C4 bus) is one of the larger of these GEO satellites and showed a signal which may be consistent with a satellite maneuver. This signal showed peaks in the power spectrum of DOLP at: 0.028, 0.043, 0.08, 0.26Hz. The third satellite, DirecTV-15 (Eurostar-3000 bus) also contained a signal which appears to be a satellite maneuver taking place. Peak frequencies of 0.069Hz and ~0.05Hz were observed in this signal.

# 1 The Need for Hyper-Temporal Imaging

## 1.1 Sensing and Resolving Satellites Using Conventional Methods

Satellites in geostationary orbit (GEO) are not only used in many everyday technologies but also extremely important in a wide range of military applications. These GEO satellites are important for a variety of communications all over the globe and have a wide range of functions from simple radio broadcasting to weather monitoring capabilities. As such, they are extremely important to the modern world.

Yet despite this, it can actually be quite hard to monitor the health of these satellites. GEO orbit is not only farther from Earth than many other useful orbits (see *Figure 1.1* below) but space in this orbit is limited and thus coveted by many. Since the orbit is roughly 36,000 km above the equator of earth these satellites can be quite faint and difficult to resolve from ground based observations.

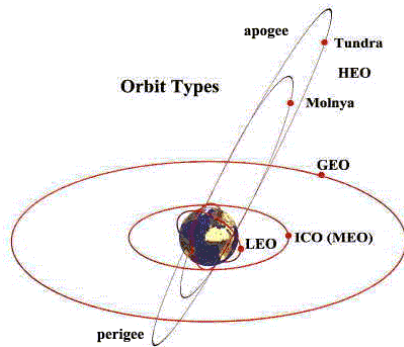


*Figure 1.1: Comparison of various Earth orbits. [7]*

Using the 6.5m MMT Observatory located on Mount Hopkins, AZ and a finely tuned adaptive optics system, Hart et al. [5] were able to resolve Telstat's Anik F2 satellite in the  $K_s$  band (infrared wavelength). It should be noted that this particular satellite contains solar panels which span 48m and is one of the largest currently in orbit. It should also be noted that the authors concluded that the solar panels of satellites such as this one could only be resolved by telescopes larger than 4m in diameter [5].

So, it is possible to resolve GEO satellites using ground based observations. However, it is difficult. Not only are there a limited number of ~4 meter class telescopes in the world, but their time is very limited and expensive. This makes it impractical to rely on such observations to monitor the health of GEO satellites.

One possible solution to this problem is to use Hyper-Temporal Imaging (HTI) to capture light curves of these objects over time. Essentially, this method utilizes acoustic imaging in order to

determine movements and features of GEO satellites without the need to resolve them spatially. *Figure 1.2* below shows the results of observations made by Hart et al. [5]. These high temporal resolution light curves show clear signals relating to the motions of two separate objects (a falling rocket body and a small satellite). The HTI instrument discussed in this document goes one step further and uses polarization as a method to further distinguish GEO satellites.

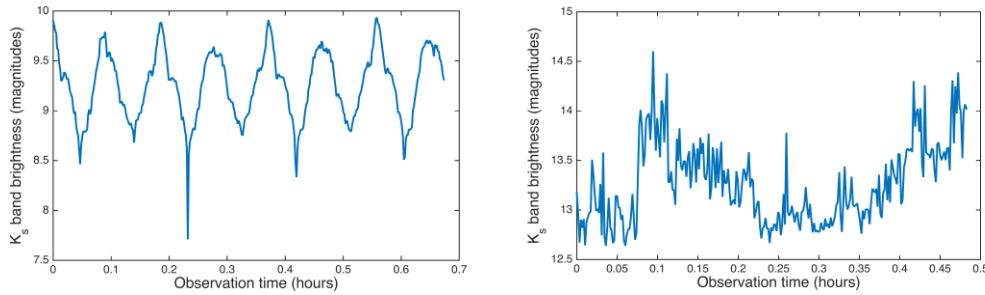


*Figure 1.2: Temporal light curves taken with MMT observations in the Ks band [5]. Left: Light curve of a tumbling Delta IV rocket body. Right: Light curve of a small satellite at GEO range. [5]*

## 1.2 Polarization and Satellites, Background

Previous work has been done to measure high temporal resolution light curves of a tumbling rocket body and a GEO satellite [5] (*Figure 1.2*). This technique demonstrated the basic idea behind this latest HTI instrument. That is, it was possible to see fluctuations in the light curves which could be related to the motions of each of these objects.

The basis of the HTI instrument described in this document expands on this work, using the idea that reflective surfaces on GEO satellites will create reflections which have some measurable degree of polarization [11]. Working under the assumption that these surfaces are connected to the satellite body in a mostly rigid way, detections in the change in this reflected, partially polarized signal over time can be tied to satellite motions and maneuvers.

In order to measure the changes in this polarization, satellite light is collected and sent through a polarizing beam splitter. Incoming partially linearly polarized light from the satellite is split into its orthogonal basis modes (s and p polarization modes). The two orthogonally polarized channels of light can then be collected simultaneously by detectors on each branch [11].

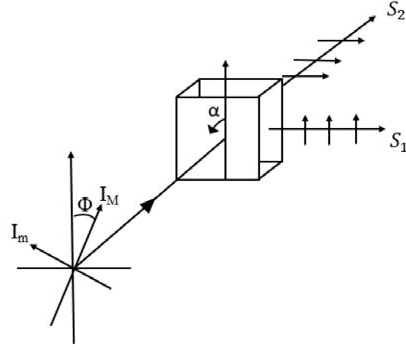


Figure 1.3: [11] Incoming linearly polarized light sent through a polarizing beam splitter is divided into two signals,  $S_1$  and  $S_2$ , which are orthogonally polarized to each other. Here  $S_1$  represents the s-mode and  $S_2$  represents the p-mode polarization.

By taking data in both detectors at fast exposure times, two light curves in each channel can be recorded. These can then be compared to each other in order to calculate the Degree of Linear Polarization (DOLP) of the signal. By analyzing this DOLP signal in the Fourier domain, frequencies relating to the satellite's motion can be pulled from this time series.

Because this method relies on a differential measurement of the two channels, many of the overall polarization effects can be ignored. For example, although polarization aberrations almost certainly exist in the telescope and HTI instrument, these will remain constant between the two channels of light and thus will be removed when the differential is taken.

### 1.3 Previous Implementation of HTI, Version 1

In 2017, Watson and Hart showed that it was possible to use this technique of acoustic imaging to distinguish GEO satellites from other space objects [11]. They created the first HTI instrument as a prototype and observed two different GEO satellites, then compared their signatures to those of an asteroid. A brief summary of their work is given here, as the work which follows in this document is closely based on this research, and can be considered a continuation of their research.

The prototype HTI instrument was used in conjunction with the 61" Kuiper telescope to collect data on two satellites, AMC-16 and Star One B4 [11]. They collected two channels of light simultaneously, in both S and P linear polarization modes. By comparing these two channels, they were able to create graphs of the degree of linear polarization (DOLP) (see Figure 1.4) [11].

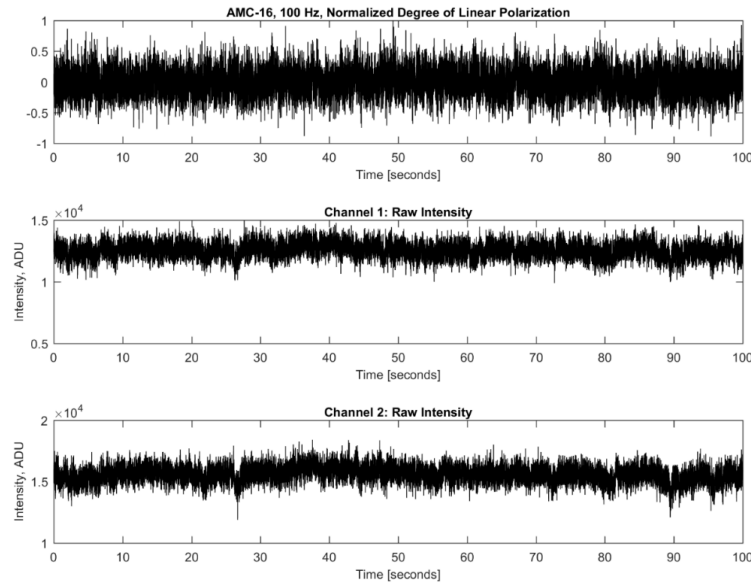


Figure 1.4: (Top) Normalized time-series DOLP measurement. (Middle and bottom) Raw photometry channels with observed fluctuations attributable to scintillation and changes in solar phase angle. These plots represent 100 seconds of data recorded at an imaging cadence of 100 Hz for AMC-16. [11]

This DOLP signal was then further analyzed in order to find and pull out artifacts relating to the GEO satellites. They calculated and compared spectrograms and acoustic power spectrum of the satellites (See figures 1.5, 1.6 below) [11].

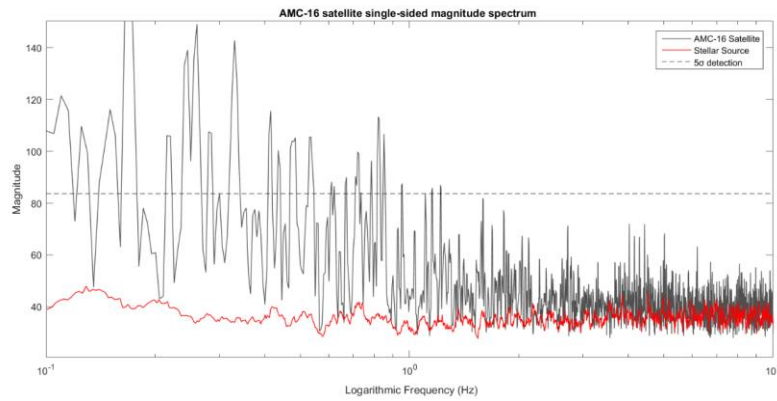


Figure 1.5: (Black) The acoustic spectrum of the AMC-16 satellite from DOLP measurements acquired in January 2017 at a rate of 100 Hz. Overlaid in red-line is the spectrum of a field stellar calibration source. [11]



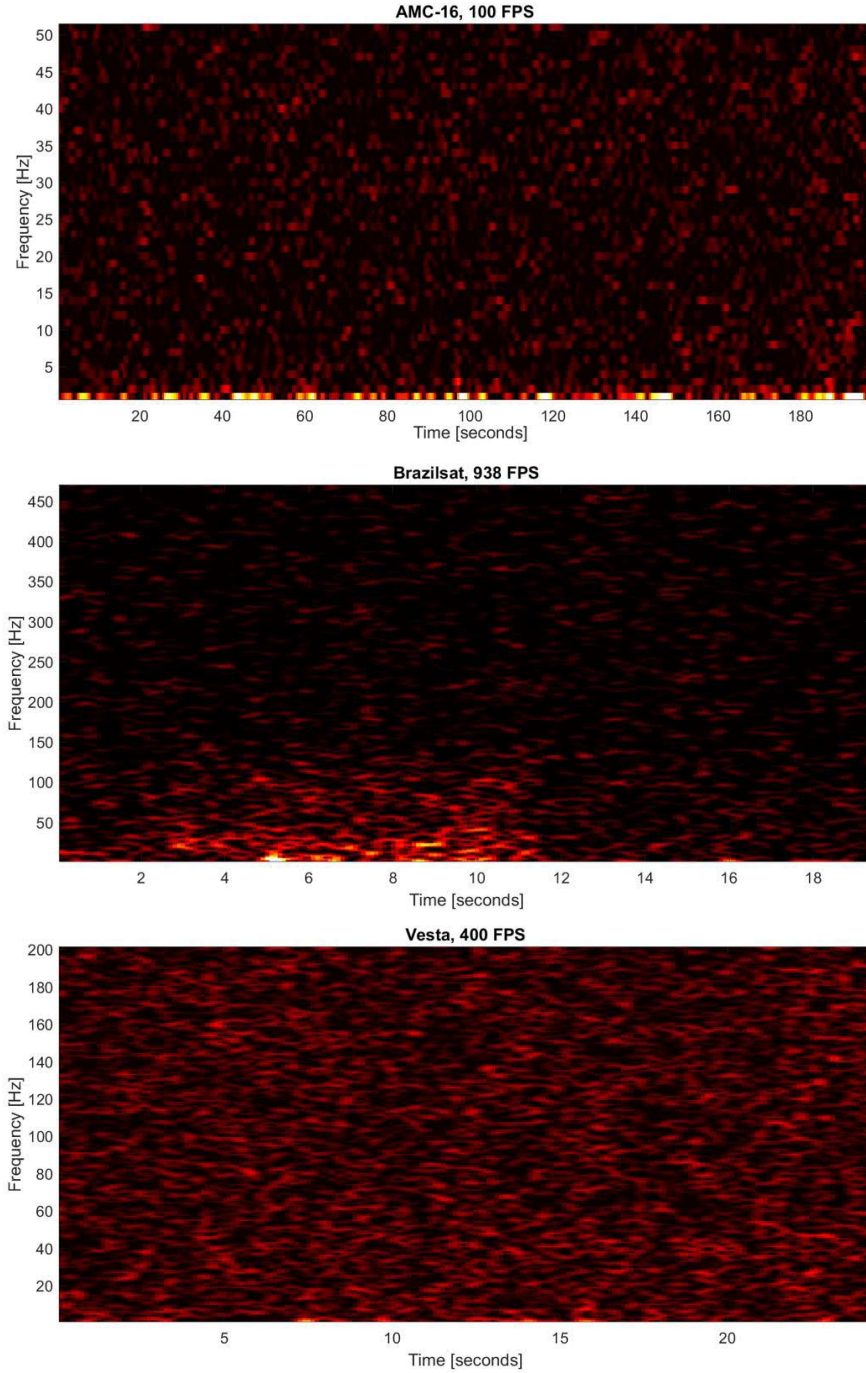


Figure 1.6: Spectrograms of (top to bottom) AMC-16 at 100 fps; Star One B4 at 938 fps; Vesta at 400 fps. The vertical scale in these plots is arbitrary and not the same in each case. [11]

From this work, they were able to say with some degree of confidence that the GEO satellites observed were in fact distinguishable from stars and asteroids based on the low frequency artifacts seen [11]. However, these observations were limited by the instrument itself. The

detectors used were very noisy (Detector readnoise of  $\sim 7$  electrons [14]), there were optical aberrations present, and their field of view was very small [11].

Due to the limitations of the first iteration of the HTI instrument, an upgrade was necessary. The purpose of this upgrade is to improve upon the ideas set forth by Watson and Hart [11]. The newest HTI instrument aims to show that different kinds of satellites have acoustic signatures that are not only distinguishable from stars and asteroids, but also distinguishable from one another.

## 2 HTI Upgrade Design

### 2.1 The Telescope and Site

Like its predecessor, the new HTI instrument has been designed to work in conjunction with the University of Arizona's 61" Kuiper telescope, located on Mount Bigelow. This site was chosen for several reasons. However, the most important reason was simply that it was possible to secure several nights of time on this telescope relatively quickly and easily.

The HTI observations relied on looking at GEO satellites whose estimated brightness can be approximated at roughly  $\sim 8\text{-}14^{\text{th}}$  magnitude (in V band) [4]. Even during bright nights (with a full moon present), the HTI instrument was estimated to be sensitive enough to be able to acquire a signal to noise ratio of at least 10. Most other astronomical observations require that the sky is dark, and thus this so called 'bright time' (those few nights around the full moon) remained undersubscribed on the 61".

Acquiring time on any scientific telescope can be difficult. However, since the Kuiper telescope was (and still is) undersubscribed during bright time it was relatively simple to apply for those nights which were undesirable to most other astronomers. The HTI project was given two nights in each of the months of May, July, August, September, October, and December for a total of 12 nights of telescope time. The details of these observations can be found in Section 4.

The Kuiper telescope is a 1.54m diameter Cassegrain telescope with an f/13.5 secondary mirror (see *figures 2.1, 2.2 and Table 2.1, 2.2* for specifications and Zemax model of the telescope)[16][17]. It is somewhat unique in that it is mounted on an equatorial fork mount which has a limit of roughly 65deg North [16][17]. Since by definition GEO satellites are stationed over the equator (roughly), this means that all of the science targets were located in the South, and not affected by this telescope limitation.

Typical good seeing conditions can be estimated to be  $\sim 1''$  with average conditions considered to be from 1-2" [16] [17]. Thus the upgraded HTI instrument has been designed to produce aberrations no larger than this atmospheric smear and to work in conjunction with these telescope optics.

# Kuiper 61" Specifications

Location Specifications	
Longitude	-110.7345
Latitude	32.4165
Elevation	8235 ft.
Telescope Specifications	
Aperture	1.54 m
Focal Length	9.6 m
Mount	Equatorial with limit of 65-degrees N

Figure 2.1: Kuiper Telescope Specifications [17]

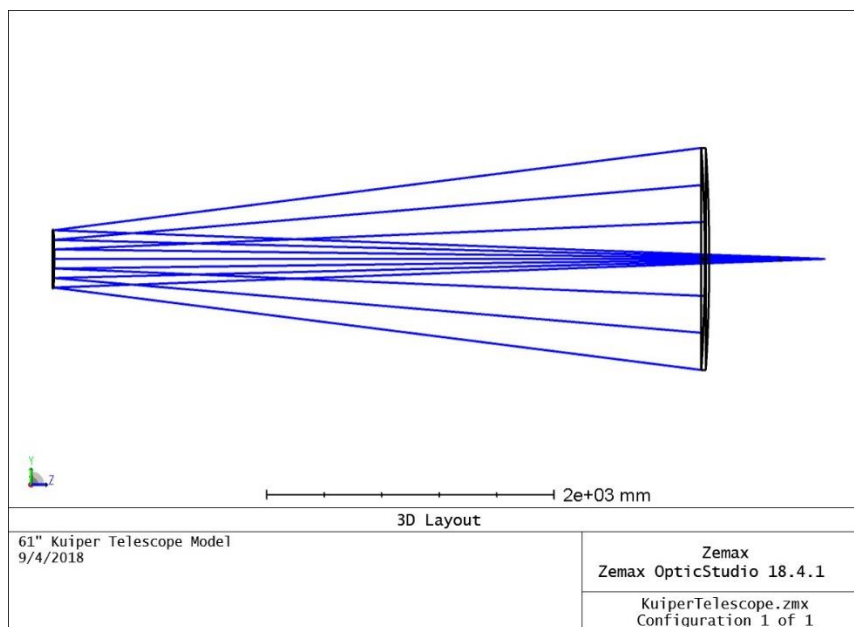


Figure 2.2: Zemax model of the Kuiper Telescope.

Table 2.1: Zemax Lens Data for 61" Kuiper Telescope Model

Surfaces :	4
Stop :	1
System Aperture :	Entrance Pupil
Diameter =	1541.48
Fast Semi-Diameters :	On
Field Unpolarized :	On
Convert thin film phase to ray equivalent :	On
I/E Conversion Method :	X Axis Reference
Glass Catalogs :	SCHOTT OHARA
Ray Aiming :	Off
Apodization :	Uniform, factor = 0.0
Reference OPD :	Exit Pupil
Paraxial Rays Setting :	Ignore Coordinate Breaks
Method to Compute F/# :	Tracing Rays
Method to Compute Huygens Integral :	Auto
Print Coordinate Breaks :	On
Multi-Threading :	On
OPD Modulo 2 Pi :	Off
Temperature (C) :	2.00E+01
Pressure (ATM) :	1.00E+00
Adjust Index Data To Environment :	Off
Effective Focal Length :	20811.46
Back Focal Length :	5364.912
Total Track :	5364.912
Image Space F/# :	13.501
Paraxial Working F/# :	13.501
Working F/# :	13.50591
Image Space NA :	0.03700893
Object Space NA :	7.71E-08
Stop Radius :	770.738
Paraxial Image Height :	1.452914
Paraxial Magnification :	0
Entrance Pupil Diameter :	1541.476
Entrance Pupil Position :	0
Exit Pupil Diameter :	507.8107
Exit Pupil Position :	-6855.951
Field Type :	Angle in degrees
Maximum Radial Field :	0.005656854
Primary Wavelength [μm] :	0.65
Angular Magnification :	3.035533
Lens Units :	Millimeters
Source Units :	Watts
Analysis Units :	Watts/cm^2
Afocal Mode Units :	milliradians

*Table 2.2: 61" Kuiper Telescope specifications from Zemax model. Units in [mm]*

	Object Space	Image Space
Focal Length :	-20811.46263	20811.4626
Focal Planes :	63173.87612	0
Principal Planes :	83985.33875	-20811.4626
Anti-Principal Planes	42362.41348	20811.4626
Nodal Planes :	83985.33875	-20811.4626
Anti-Nodal Planes	42362.41348	20811.4626
WFNO:		13.5059
ENPD:		1541.48
TOTR:		5364.91

Future options exist to adapt this HTI instrument to other telescopes such as the 90" Bok telescope on Kitt peak. However, this has yet to be implemented. For the purposes of this report, only the 61" Kuiper telescope has been used. All observations referred to here can be assumed to have been taken at this site.

## 2.2 Optical Design of HTI Upgrade

The original HTI instrument was limited by noise and a rather small field of view. Thus a new instrument was designed to improve upon these problems.

### 2.2.1 Light Path and Lens System

Figure 2.3 gives a comparison of the original optical layout of the HTI instrument compared to the newest HTI upgrade. Notable additions to the optical design include the addition of a field lens (L1), larger fold mirrors (M3 and M4), and newly designed final imaging lenses (L3). Figure 2.4 shows the path of the s-mode polarized light in the newest upgrade, as modeled in Zemax.

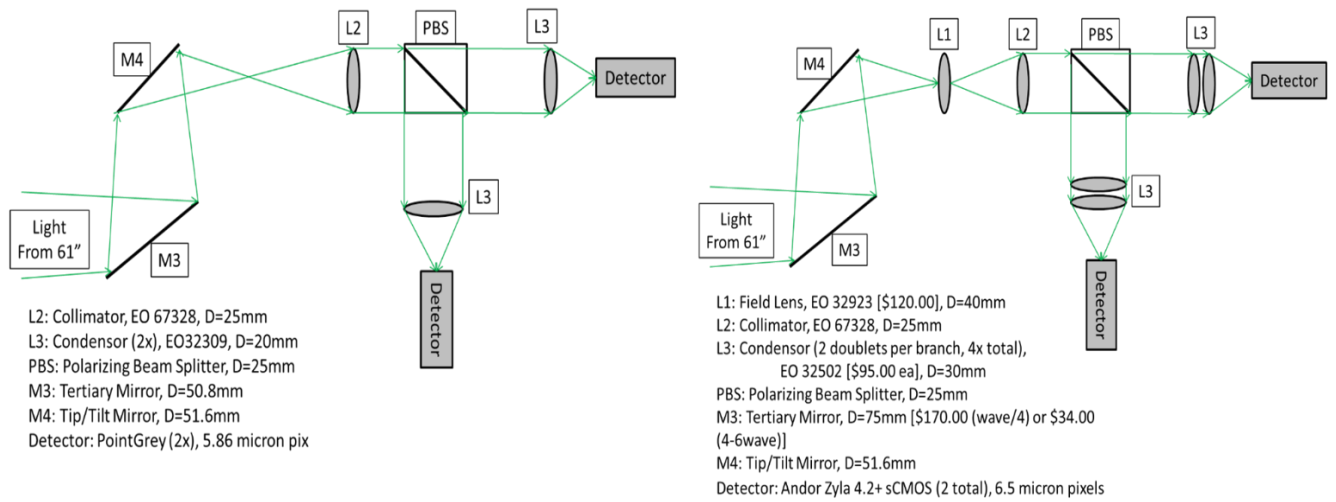


Figure 2.3: Cartoon comparison of HTI 1<sup>st</sup> Generation and Upgraded layouts. Left: 1<sup>st</sup> Generation of HTI. Right: HTI Upgrade Optical Layout

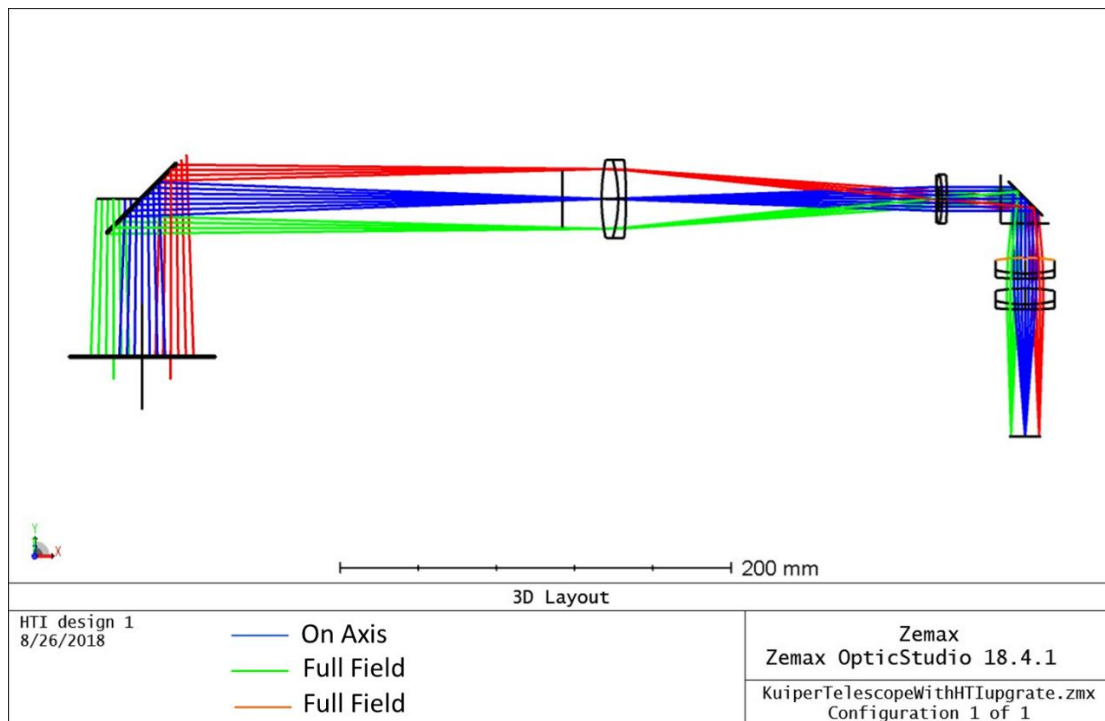
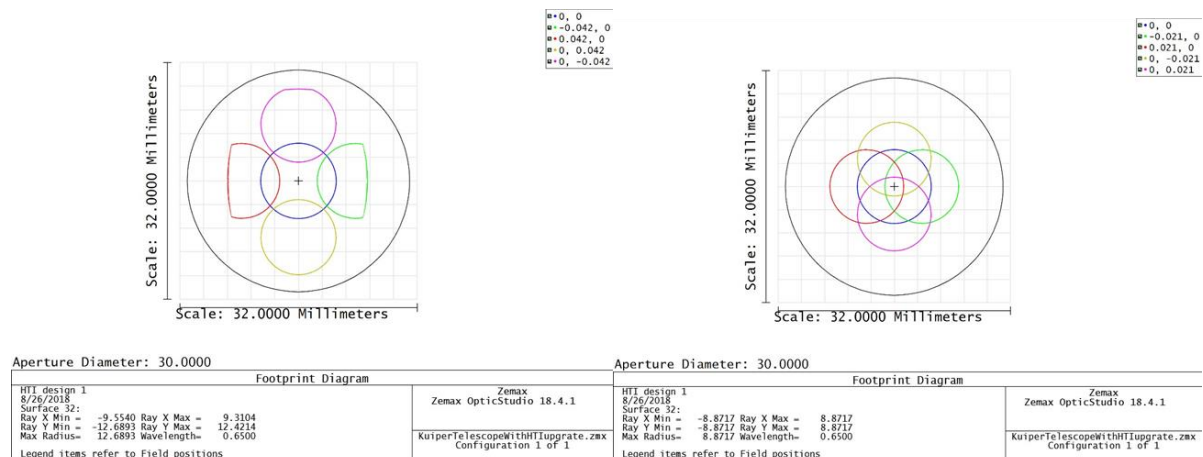


Figure 2.4: Top down view of the Optical Layout of HTI Upgrade as modeled in Zemax. The first element shown is M3. In place of the polarizing beam splitter, a simple fold mirror has been used to model the light path. This diagram shows the reflected path of that beam splitter, or s-mode polarized light path. Red and Green rays represent full field, which is modeled as 2.5 arcminutes off axis (for a total FOV of 5 arcminutes).

The addition of L1 gives an improved field of view. Larger diameter M3/M4 mirrors serve to reduce vignetting in the system and allow for the increased FOV. These mirrors serve the same purpose as in the original design, that is as a periscope to align the optical axis of HTI to that of the 61" Kuiper telescope. The first generation HTI instrument had large amounts of both spherical aberration and coma present, mainly in the final lens (L3). Therefore the newest L3 lenses have been designed to reduce these two optical aberrations in the image while maintaining the achromatic design present in the first generation. Finally, the detectors have been mounted on electronic stages which can be moved along the optical axis as needed in order to focus the instrument.

A Zemax model (see figure 2.5) of the instrument shows that over a 5 arcminute full field of view, 99.6764 percent of the light will remain unvignetted and total aberrations at the edge of the field will remain under 5 waves of error. In the visible spectrum (wavelength assumed to be 588nm), 5 waves corresponds to approximately 0.0633 arcseconds of blur on the Andor Zyla detectors (with similar values for the Grasshopper detector configuration). The figures (2.5 and 2.6) and tables (2.3, 2.4, 2.5, 2.6) below show multiple metrics to measure optical clarity of the newest design, as modeled by Zemax.





Full Field 2.5'

Half Field 1.25'

*Figure 2.5: Footprint vignetting diagram at the last lens surface. Note that at full field, some vignetting is present in the horizontal-direction due to the 45 degree angle of M4. This was unavoidable due to space constraints of the optomechanics.*

Site conditions at the Kuiper telescope are the expected limiting factor in these observations. Seeing in the visible spectrum can be expected to be approximately ~1 arcsecond [16] (as shown in section 2.2). Thus the system has been designed to operate with aberrations less than this expected seeing value. As shown below, models indicate that even at the full field of 5 arcminutes, aberrations should be well within the natural seeing limit of the site.

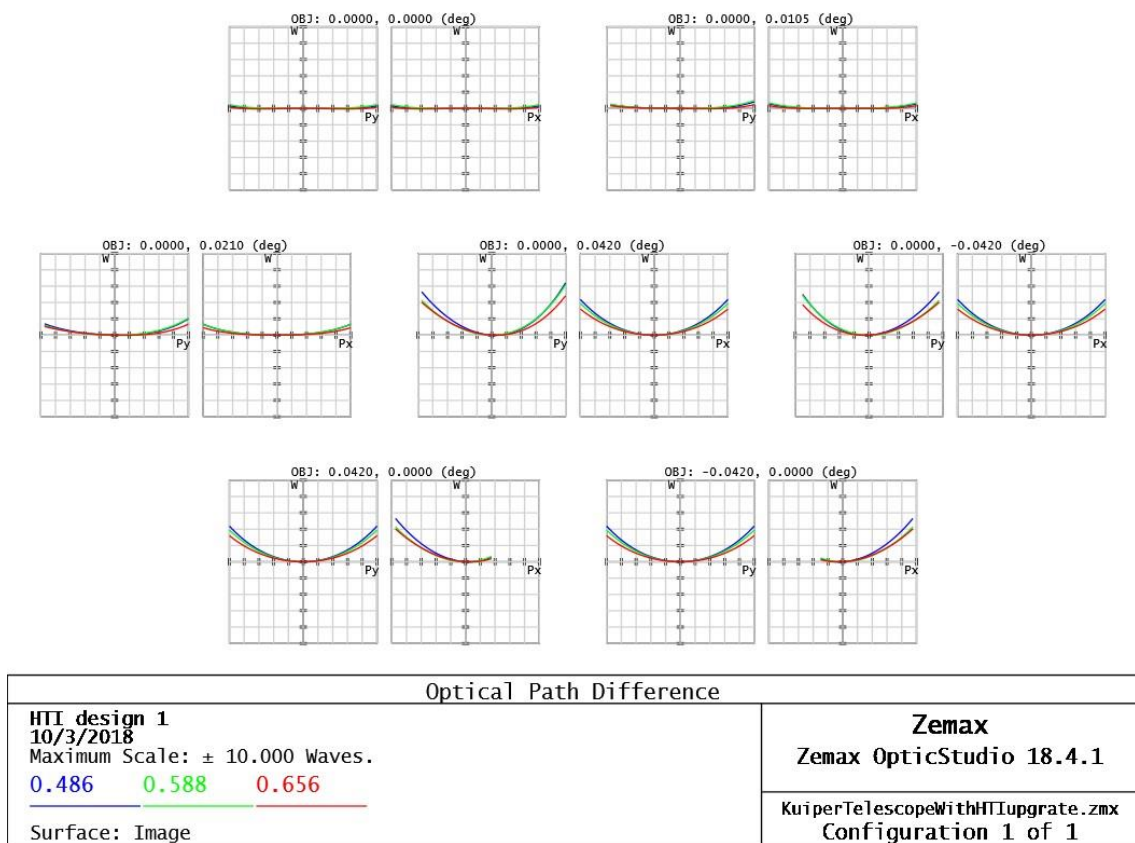


Figure 2.6: Optical Path Differences in HTI. Plotted as modeled in Zemax.

Table 2.3: Total Wavefront Aberration Coefficients. Calculated using F,d,C wavelengths in Zemax.

Wavefront Aberration Coefficient Summary [Waves]:							
	W040	W131	W222	W220P	W311	W020	W111
TOT	0.4865	0.7084	1.6035	2.5856	3.9137	-0.1443	-0.3839
	W220S	W220M	W220T				
TOT	3.3874	4.1891	4.9909				

Table 2.4: Seidel Coefficients at each surface in waves. Calculated using F,d,C wavelengths in Zemax.

Seidel Aberration Coefficients in Waves:								
Surf	W040	W131	W222	W220P	W311	W020	W111	Name
STO	0	-3.84011	0.044544	-0.022272	0	0	0	PRIMARY Mirror
2	-0.06723	3.505912	-0.004999	0.061081	-0.00115	0	0	SECONDARY Mirror
3	0	0	0	0	0	0	0	
4	0	0	0	0	0	0	0	tertiary mirror (M3)
5	0	0	0	0	0	0	0	
6	0	0	0	0	0	0	0	
7	0	0	0	0	0	0	0	
8	0	0	0	0	0	0	0	tipt tilt mirror (M4)
9	0	0	0	0	0	0	0	
10	0	0	0	0	0	0	0	set to 0 for initial design
11	0.000017	-0.000293	0.001242	0.469036	-3.97529	-0.00047	0.004015	EO 32923 (L1)
12	0.000127	0.006199	0.075413	-0.117996	-1.95358	-0.04165	-1.01351	EO 32923 (L1)
13	-0.00181	-0.034026	-0.159866	0.265511	1.743803	0.111532	1.048022	EO 32923 (L1)
14	0	0	0	0	0	0	0	focal plane 1
15	0	0	0	0	0	0	0	
16	0.376674	1.512656	1.518638	0.431671	2.391401	-2.56739	-5.15508	EO 67328 (L2)
17	-0.09661	0.261525	-0.176992	-0.122914	0.286151	4.804891	-6.50359	EO 67328 (L2)
18	0.016039	-0.159672	0.397392	0.304754	-2.50597	-2.35015	11.69812	EO 67328 (L2)
19	0	0	0	0	0	0	0	
20	0	0	0	0	0	0	0	
21	0	0	0	0	0	0	0	
22	0	0	0	0	0	0	0	PBS edge approximation
23	0	0	0	0	0	0	0	
24	0	0	0	0	0	0	0	EDO 25mm PBS
25	0	0	0	0	0	0	0	
26	0	0	0	0	0	0	0	PBS edge approximation
27	0.071525	0.746274	1.946608	0.506792	7.721476	-1.7335	-9.04348	1st EDO 32502 (L3)
28	-0.27659	-0.720877	-0.469707	-0.127282	-0.47192	6.032646	7.861461	1st EDO 32502 (L3)
29	0.213001	-0.103359	0.012539	0.278863	-0.06918	-4.3772	1.062024	1st EDO 32502 (L3)
30	-0.00432	-0.114759	-0.762271	0.506792	1.669314	-0.48111	-6.39139	2nd EDO 32502 (L3)
31	-0.41387	-1.449942	-1.269915	-0.127282	-1.3352	6.093698	10.67419	2nd EDO 32502 (L3)
32	0.669541	1.098866	0.450871	0.278863	0.413833	-5.63563	-4.62466	2nd EDO 32502 (L3)
33	0	0	0	0	0	0	0	Andor Zyla Detector
IMA	0	0	0	0	0	0	0	
TOT	0.4865	0.708393	1.603499	2.585618	3.913706	-0.14435	-0.38387	

Table 2.5: Cardinal Points from Zemax model of HTI

	Object Space	Image Space
Focal Length :	9812.753205	9812.753205
Focal Planes :	-61883.08373	0
Principal Planes :	-71695.83694	-9812.753205
Anti-Principal Planes :	-52070.33053	9812.753205
Nodal Planes :	-52070.33053	9812.753205
Anti-Nodal Planes :	-71695.83694	-9812.753205

Table 2.6: Zemax Lens Data for HTI instrument.

Surfaces :	34
Stop :	1
System Aperture [Entrance Pupil Diameter] :	1541.48
Fast Semi-Diameters :	On
Field Unpolarized :	On
Convert thin film phase to ray equivalent :	On
I/E Conversion Method :	X Axis Reference
Glass Catalogs :	SCHOTT OHARA
Ray Aiming :	Off
Apodization :	Uniform, factor = 00
Reference OPD :	Exit Pupil
Paraxial Rays Setting :	Ignore Coordinate Breaks
Method to Compute F/# :	Tracing Rays
Method to Compute Huygens Integral :	Auto
Print Coordinate Breaks :	On
Multi-Threading :	On
OPD Modulo 2 Pi :	Off
Temperature (C) :	2.00E+01
Pressure (ATM) :	1.00E+00
Adjust Index Data To Environment :	Off
Effective Focal Length :	-9812.753
Effective Focal Length (In image space) :	-9812.753
Back Focal Length :	-64.70876
Total Track :	5421.597
Image Space F/# :	6.365816
Paraxial Working F/# :	6.365816
Working F/# :	6.361977
Image Space NA :	0.07830336
Object Space NA :	7.71E-08
Stop Radius :	770.738
Paraxial Image Height :	7.193125
Paraxial Magnification :	0
Entrance Pupil Diameter :	1541.476
Entrance Pupil Position :	0
Exit Pupil Diameter :	240.3252
Exit Pupil Position :	-1529.866
Field Type :	Angle in degrees
Maximum Radial Field :	0.042
Primary Wavelength [μm] :	0.5875618
Angular Magnification :	-6.306394
Lens Units :	Millimeters
Source Units :	Watts
Analysis Units :	Watts/cm^2
Afocal Mode Units :	milliradians
MTF Units :	cycles/millimeter

### 2.2.2 Detector Specifications (2 Different Configurations: Flir Grasshopper and Andor Zyla)

Upgrades to the system have been made in essentially two steps, mostly due to delays in shipment. Although the optical path and layout remains the same in each instance of the HTI Upgrade, the detectors were changed. This resulted in two different configurations, each with its own set of detectors: The original detectors were Flir Grasshopper3-U3, and the second set of detectors were Andor Zyla 4.2+ sCMOS. Below are listed the detector specifications for each of these sets of detectors in combination with the optical components mentioned in the previous section.

The pixel size of each of these detectors is different, however the optics remain the same in both configurations. Thus there are different plate scales for each of these different detector configurations. The calculations for plate scale can be found according to *EQUATION 2.1* for each of these cases. For the same reason, the field of view (FOV) will change slightly with each different detector. These calculations can be seen below in *EQUATION 2.2*. The results of these calculations are shown below for each of the different detectors.

$$\text{EQUATION 2.1} \quad \text{PlateScale [arcsec/pixel]} = 206.265 * \frac{\text{PixelSize } [\mu\text{m}]}{F_{\text{Telescope}} [\text{mm}]}$$

$$\text{EQUATION 2.2} \quad \text{FOV [arcsec]} = \text{PlateScale[arcsec/pixel]} * \text{TotalPixels}$$

Although the detectors may have changed once, several design specifications remain the same. For instance, there are always two separate channels of light, each with a detector. Each detector sees the same object in orthogonally polarized (S and P) light. Each detector runs simultaneously in order to capture two synchronized streams of data. In all configurations, one detector is used to trigger the other so that the data streams start simultaneously. Images are then recorded at a rate of 4-1000 frames per second (fps) depending on what is allowed by sky conditions and target magnitude. These two streams can then be analyzed in order to determine various acoustic features of each target [11]. See the section 4 for complete data analysis techniques.

### **Detector Set 1: Flir/Point Grey Grasshopper3: GS3-U3-23S6M-C**

The original HTI instrument [11] was created to be as cost effective as possible. It therefore used optical components and detectors which were both cheap and easily accessible. Since this was only meant as a proof of concept for the instrument, this worked acceptably well. The two detectors present in this design were Flir Grasshopper3 models. Due to delays in shipping, our newest upgrade made use of these same detectors during the first observation run in May. The specifications can be seen below in *figure 2.6* below.

Plate Scale: 0.12311 [arcsec/pix]

Full Field of View Horizontal: 3.939673 [arcmin]

Full Field of View Vertical: 2.462296 [arcmin]

Read noise: 6.8 electrons

#### **Point Grey GS3-U3-23S6M-C**

Sensor Type	sCMOS
Active Pixels	1920 x 1200 (2.3 Megapixel)
Sensor Size	11.3 x 7.0 mm (13.3 mm diagonal)
Pixel Size	5.86 $\mu$ m
Pixel readout rate	300 Mpix/s
Read Noise (e-)	6.8
ADC	12 bit (Mode 7)

#### **Frame rate**

<b>Array Size</b>	<b>Frames/sec</b>
1920x1200	128
1280x960	158
416x240	546
192x120	923



13

*Figure 2.6: Flir/Point Grey Grasshopper3 Detector Specifications and maximum frame rates [14]*

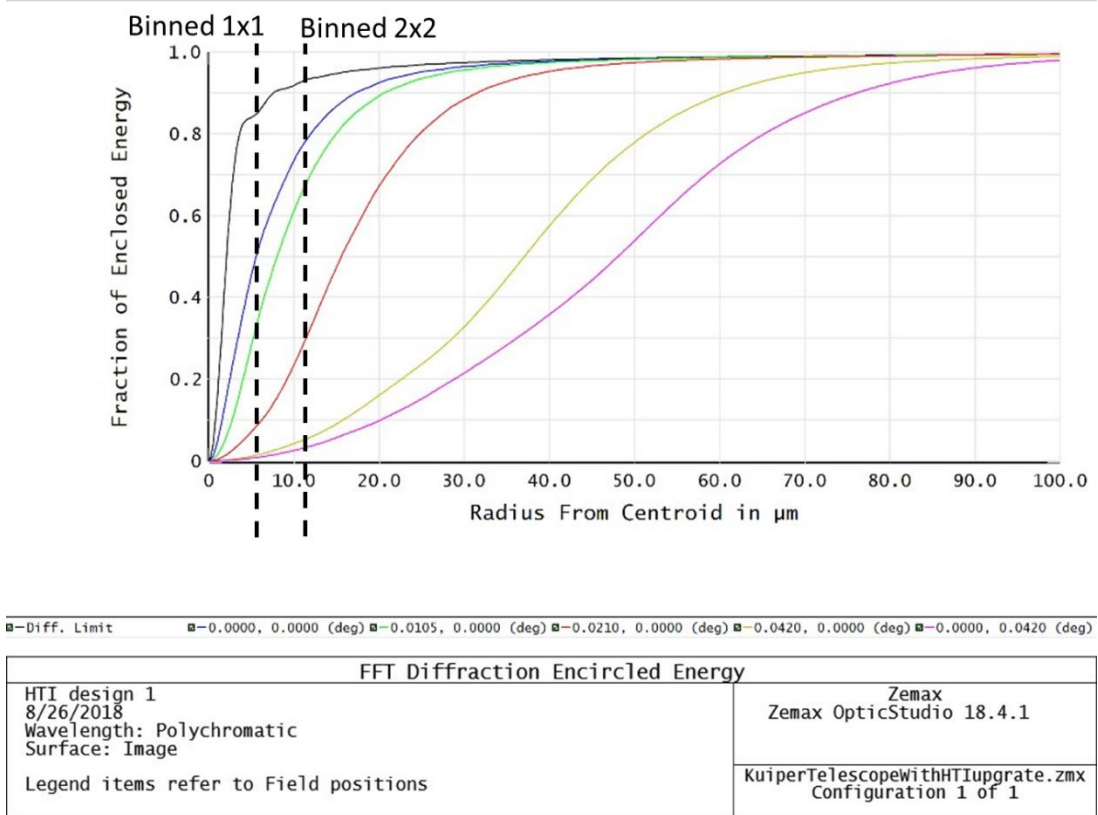


Figure 2.7: Encircled energy for Flir Grasshopper pixel scale over a range of fields ranging from: on-axis (black), quarter field (blue/green), half field (red), to 2.5' full field (yellow/purple).

## Detector Set 2: Andor Zyla 4.2+ sCMOS

The second model of detectors are Andor Zyla 4.2+ sCMOS. These Andor Zyla detectors are capable of maximum readout speeds ranging from 53 frames per second (fps) at full-frame to a top speed of 1578 fps when reading out a 128x128 array. By choosing the correct binning and frame, it is possible to reach readout speeds greater than 1000 frames per second. These detectors provide a much needed improvement in both noise and speed from the previous Grasshoppers.

Plate Scale: 0.13656 [arcsec/pix]

Full Field of View: 4.66127 [arcminute]

Note: the Zyla detectors contain square sensors, so horizontal and vertical FOV are the same.

Read Noise: ~0.9-1.1 electrons (depending on readout speed)

### Detector Specifications

Sensor Type	Front Illuminated Scientific CMOS (4T) – sCMOS 2.0
Active Pixels	2048 x 2048 (4.2 Megapixel)
Sensor Size	13.3 x 13.3 mm (18.8 mm diagonal)
Pixel Size	6.5 $\mu\text{m}$
Pixel readout rate (MHz)	Fast Read 540 (270 MHz x 2 sensor halves) Slow Read 216 (106 MHz x 2 sensor halves)
Read Noise (e-)	
216 MHz	0.9
540 MHz	1.10
Maximum frame rate	53 fps @ full frame (USB 3.0) 100 fps @ full frame (Camera Link 10-tap)
Maximum Quantum Efficiency	82%
Dark current, e-/pixel/sec @ 0°C	0.10

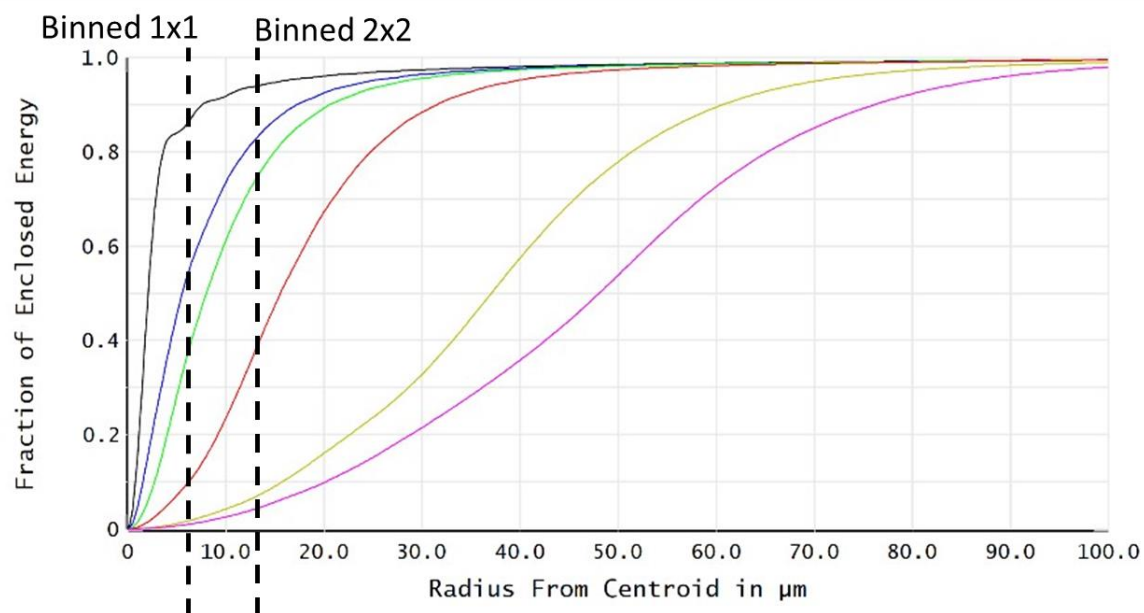
### Frame rate

Array Size	Frames/sec
2048x2048	53
1920x1080	107
512x512	403
128x128	1578



Figure 2.8: Andor Zyla 4.2+ sCMOS detector specifications [13] and maximum frame rates.





■ - Diff. Limit    ■ - 0.0000, 0.0000 (deg)    ■ - 0.0105, 0.0000 (deg)    ■ - 0.0210, 0.0000 (deg)    ■ - 0.0420, 0.0000 (deg)    ■ - 0.0000, 0.0420 (deg)

FFT Diffraction Encircled Energy	
HTI design 1 8/26/2018 Wavelength: Polychromatic Surface: Image	Zemax Zemax OpticStudio 18.4.1
Legend items refer to Field positions	KuiperTelescopeWithHTIupgrade.zmx Configuration 1 of 1

Figure 2.9: Encircled energy for Andor Zyla pixel scale over a range of fields ranging from: on-axis (black), quarter field (blue/green), half field (red), to 2.5' full field (yellow/purple).

## 3 HTI on the Telescope

### 3.1 Experimental Design - Aim of the Observations

Several GEO satellites were chosen prior to each telescope run as potential targets to observe. There were three main factors which determined the choice of target.

The first and most important factor was based on the satellite proximity to the site, and thus location in the sky. If a satellite is located above the equator (0 degrees latitude) and the 61" telescope is located at 32 degrees latitude, then by definition the highest that any of these objects could possibly be is 58 degrees above the horizon. In reality, this quick calculation does not account for the fact that GEO orbit is not at infinity. When parallax is considered, the highest a GEO object could be above the horizon is actually about 5 degrees lower (or ~53 degrees elevation). It is not possible to observe any object lower than 15 degrees above the horizon with the Kuiper telescope, and not desirable to observe targets lower than about 30 degrees in elevation, so it became important to locate potential targets which were stationed not more than ~38 degrees (ideally less than ~30 degrees) away from the telescope site longitude of -110W in Arizona.

The next factor was simply to choose satellites which had already been observed by the first iteration of HTI. These two were AMC-16 and StarOne/Brasilsat B4 [11]. And finally the last factor in target choice was to choose satellites which were large and thus likely to be brightest in the sky.

The goal of the observations of these satellites consists of three main components:

- 1) Characterize the upgraded optics and align the new system to the telescope axis.
- 2) Determine whether satellites can be distinguished from one another using this instrument.
- 3) Determine how other effects such as telescope tracking may be affecting the accuracy of the data.

Prior to the very first observation run, the components on HTI were carefully laser aligned in the lab. However, there was no way to align the optical axis of HTI to that of the Kuiper telescope until the first night of observations. Therefore in order to fully satisfy the 1<sup>st</sup> experimental goal, a few hours at the start of each observation run were set aside for alignment. This was done by simply pointing the telescope to a bright object (Jupiter, Altair, Vega served well) in the sky, then adjusting M3/M4 (the periscope mirrors) on HTI as needed. Adjustments to the 2ndary mirror on the telescope were also made in order to bring light into focus, as well as the individual stage mounts of each detector (which served as fine focus control for each individual camera).

To satisfy the second goal, the plan was to observe several different satellites over the course of the nights given. A number of different types of satellites were chosen to be observed. As the

satellites orbit earth, their magnitude can fluctuate greatly (From fainter than ~12 to ~8 magnitude) over the course of a night. When satellites are at opposition to the sun, they are brightest [4]. Thus each of the targets were organized into groups according to what time would they would be theoretically the brightest. Timeseries of each satellite were to be taken at the highest frame rate possible (given by the detector).

One of the concerns from the first iteration of HTI was the possibility that the telescope tracking could be interfering with observations of the satellite. Thus an experiment was devised in which data would be taken first with the telescope tracking turned on, then with the same configuration but with the telescope tracking turned off. Since the targets are geosynchronous in nature, telescope tracking would not be necessary in order to keep the target in the frame.

*Table 3.1: Potential target list (complete set)*

Observation Order (E to W)	Target Name	Type	NORAD ID	Station	Position Relative to 61"
1	AMC-16	A2100AXS	28472	84 W	EAST 36°
2	SKYM-1	GeoStar-2 Bus	40664	78.8° W	EAST 31.2°
3	SBS-6	HS-393	20872	80.9 W	EAST 29.1°
4	ARSAT-2	ARSAT-3k	40941	81 W	EAST 29°
5	Star One/Brazilsat B4	HS-376W	26469	91W	EAST 18°
6	Galaxy-17	Spacebus 3000 B3	31307	91 W	EAST 19°
7	IS-30	SSL-1300	40271	95.05° W	EAST 15°
8	AMC-4 (GE-4)	A2100AX	25954	101 W	EAST 9°
9	DirecTV 4S	BSS-601HP	26985	101.2° W	EAST 8.8°
10	DirecTV 15	Eurostar-3000	40663	102.75° W	EAST 7.2°
11	Spaceway 1	BSS-702	28644	102.925° W	EAST 7.1°
12	Americom-15 (AMC-15)	A2100AXS	28446	105 W	EAST 5°
13	AMC-18	A2100A	29644	105W	EAST 5°
14	DirecTV 5	SSL-1300	27426	110.1° W	WEST 0.1°
15	XM-4	BSS-702	29520	115.25° W	WEST 5.3°
16	Sirius FM-6	SSL-1300	39360	116.15° W	WEST 6.2°
17	Anik F3	Eurostar-3000S	31102	118.7W	WEST 8.7°
18	G-23 (Telstar 13)	SSL-1300	27854	121° W	WEST 11°
19	Galaxy 18	LS-1300 (Intelsat)	32951	123.0 W	WEST 13°
20	G-14	Star-2 Bus	28790	125° W	WEST 15°
21	AMC-1 (GE-1)	A2100A	24315	128.6 W	WEST 18.6°
22	Ciel-2	Spacebus 4000 C4 (LARGEST BUILT)	33453	128.8 W	WEST 18.8°
23	GOES-15	BSS 601	36411	135 W	WEST 25°

### 3.2 The Satellites

The following Table is a list of the various kinds of satellites on the potential target list as organized by manufacturer [18].

*Table 3.2: Manufacturer and Satellite bus types of each of the potential targets.*

	Lockheed Martin	Boeing/ Hughes	OCS/ Orbital ATK/ Northrop Grumman Innovation Systems (NGIS)	INVAP (Argentina)	Alcatel Space/ Alcatel Alenia Space/ Thales Alenia Space	Ford/ Space Systems Loral (SSL)	EADS Astrium/ Airbus Defence and Space
Manufacturer							
Bus	A2100AXS	BSS-601HP	GeoStar-2	ARSAT-3k	Spacebus 3000 B3	SSL-1300	Eurostar-3000
	A2100AX	BSS-601	Star-2		Spacebus 4000 C4		Eurostar-3000S
	A2100A	BSS-702					
		HS-393					
		HS-376W					

#### Hughes - HS-376W

Shown below in *figure 3.1* is a schematic of HS-376. This spacecraft is closely related to the HS-376W model, and can be used as a general comparison for the data collected by HTI. According to Giles et al. [4], HS-376 is a spin stabilized satellite bus with a spin period of  $\sim 1.08$  seconds. In addition, they provide a basic description of the satellite:

The outer surface of each AUSSAT satellite is covered with nearly 16 000 solar cells. The precise arrangement of these cells gets quite complicated as there are 3 main regions, several different sizes and also strips of filler cells to maximize coverage of the available surface area. A more detailed description of the solar cells on the AUSSAT spacecraft can be found in Gorian and Henry (1986). An excellent approximation is that the deploying aft section has 98 cells around its circumference and the fixed forward section has 104 (see Figure 1). These values were determined from the FFT of 4 April before the detailed drawings of the solar cell distribution arrived from Hughes. The typical cell size is about 2.3 by 6.5 cm with the long axis aligned around the circumference. Since each revolution of the satellite occurs in  $\sim 1.08$  s the reflections from the lengthwise strips of cells occur at 90 and 95.5 Hz.

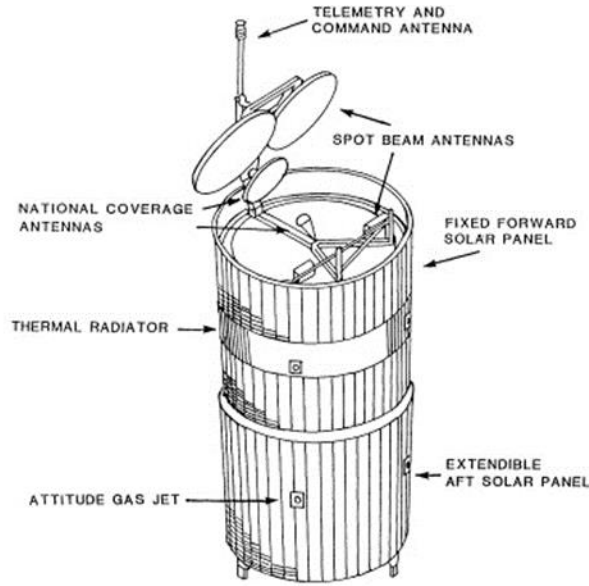


Figure 3.1: A schematic of the AUSSAT spacecraft with the aft section deployed. This is a standard Hughes HS376 model. In general the solar cells are placed in vertical strips and the individual rectangular cells are oriented with their longer axis around the satellite circumference.[4]

## BOEING

A thesis by Mohsenhizadeh [7] has studied Boeing GEO satellites and the frequencies that might be seen in their solar panel motions as they complete a maneuver. This Solar Wing Drive (SWD) movement for a satellite in GEO orbit is suggested to be 0.104Hz [7]. This is calculated as EQUATION 3.1, where  $T_{SWD}$  is taken to be 9.6 seconds [7].

$$EQUATION\ 3.1: \quad f_{SWD} = \frac{1}{T_{SWD}}$$

While this work was done specifically for Boeing satellite busses, it can be somewhat generalized for similarly shaped satellites (that is those with a small rectangle body with two large solar panel wings). Since several of the satellites on the potential target list appear similarly shaped to this bus, it's reasonable to assume that when these satellites maneuver they are likely to produce signals similar to this suggested  $f_{SWD}$ .



*Figure 3.2: Cartoon of a BSS-601 satellite bus. [15]*

### **Thales Alenia – Spacebus 4000 C4**

This is the largest of the spacebus class satellite busses manufactured by Thales Alenia. It consists of two solar panels attached to a central body.



*Figure 3.3: Manufacturer image of the Spacebus 4000C4 satellite bus [19].*

### **Airbus – Eurostar E3000**

This satellite is a somewhat standard central body with two wing-like solar panels on either side.



*Figure3.4: Cartoon of the Eurostar E3000 satellite bus [18].*

### 3.3 First Observations Using the Flir Grasshopper Detectors (May)

These observations served mostly as a first light commissioning run. A large portion of the time during these first two nights was spent aligning the optical axis of HTI to that of the Kuiper telescope. Data was taken on several satellites and a few stars during these May nights. However, the data was not suitable for analysis and thus is not presented here.

This run did however show that the instrument worked as it was designed to do. First light was achieved, as shown in the figure below.

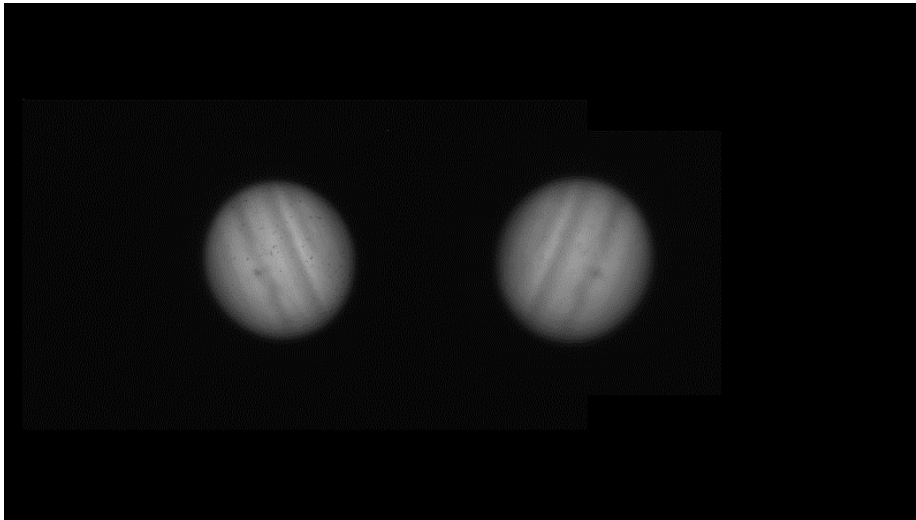


*Figure 3.3: First light image of Jupiter taken May 30, 2018. Two images shown in both  $s$  and  $p$  polarization channels simultaneously.*

### 3.4 Second Observations using the Andor Zyla Detectors (July, Aug, Sept, Oct)

Observations over July 21 and 22 were mostly clouded out. None of the July data is analyzed here.

During August 28 and 29, data was taken on 10 different satellites and 4 bright ( $m_V \sim 4-5$ ) stars. Each series was  $\sim 1-5$  minutes in length. Data was first taken with telescope tracking turned on, then a similar set was taken with the tracking turned off. Data was taken at frame rates which allowed for a signal to noise ratio of roughly 10 in each image. The second of these two nights was partly lost due to clouds, but data was collected on the first night successfully.

On September 25 and 26, data was taken on 5 target satellites. These data were taken over as long a period of time as the detectors would allow without overheating. These continuous timeseries lengths ranged from just under 5 minutes to 20 minutes. These longer times were chosen in the hopes of maximizing the chance that our observations would catch a satellite



maneuver in progress. Telescope tracking was turned off for most satellites while data was taken.

Satellite brightness did not remain constant throughout the night, despite the good weather. In several cases, the satellites would fade out completely (presumably as their solar panels turned away from the sun) and in others the overall intensity increased with time (presumably as the satellite turned towards the sun). Data was taken at frame rates which allowed for a signal to noise ratio of roughly 10 in each image. Data on all but one satellite (NORAD ID 26469) were taken with the telescope tracking turned off so as to minimize vibrations which might be caused by the telescope.

In addition to the satellite data, timeseries were taken on four different stars (two on the first night, two on the second) as well. The two stars on the first night were both bright ( $mV \sim 4-5$ ) while on the second night one was bright and the other was faint ( $mV \sim 11.5$ ). These were taken over a much shorter timespan, and were taken with the sidereal telescope tracking turned on.

Observations in October (10/20 and 10/21) consisted of data taken on the same five satellites plus two more and plus two new faint stars ( $mV = \sim 11.5$ ). A similar method of collection to that of the September run was used during these two nights, however clouds and bad weather limited the observations.

## 4 Data analysis

There are two possible signals which could be detected in these GEO satellites. The first signal is simply the signal which the satellite creates as it moves naturally. This is expected to be relatively constant over a long period of time. The second expected signal is that which is associated with a satellite maneuver. This is expected to be only a few seconds to a few minutes in length. These are partially described in section 3.2 above.

### 4.1 Basic Outline

Data was taken on a variety of satellites (see *table 4.1*) over a total of 10 nights. Several timeseries of data were recorded for each of these satellites in the two cameras simultaneously. These timeseries were then individually analyzed and compared to one another using the following methods.

*Table 4.1: Target list of satellites actually observed. Note that although a large amount of satellites were observed, only a few are analyzed in depth here. In many, the data was either not interesting, too noisy, or simply bad and thus not worth analyzing further.*

Observation Order (E to W)	Target Name	Type	NORAD ID	Station	Position Relative to 61"
1	AMC-16	A2100AXS	28472	84 W	EAST 36°
2	SKYM-1	GeoStar-2 Bus	40664	78.8° W	EAST 31.2°
3	Star One/Brazilsat B4	HS-376W	26469	91W	EAST 18°
4	Galaxy-17	Spacebus 3000 B3	31307	91 W	EAST 19°
5	IS-30	SSL-1300	40271	95.05° W	EAST 15°
6	AMC-4 (GE-4)	A2100AX	25954	101 W	EAST 9°
7	DirecTV 4S	BSS-601HP	26985	101.2° W	EAST 8.8°
8	DirecTV 15	Eurostar-3000	40663	102.75° W	EAST 7.2°
9	Spaceway 1	BSS-702	28644	102.925° W	EAST 7.1°
10	Americom-15 (AMC-15)	A2100AXS	28446	105 W	EAST 5°
11	AMC-18	A2100A	29644	105W	EAST 5°
12	DirecTV 5	SSL-1300	27426	110.1° W	WEST 0.1°
13	XM-4	BSS-702	29520	115.25° W	WEST 5.3°
14	Sirius FM-6	SSL-1300	39360	116.15° W	WEST 6.2°
15	Anik F3	Eurostar-3000S	31102	118.7W	WEST 8.7°
16	G-23 (Telstar 13)	SSL-1300	27854	121° W	WEST 11°
17	G-14	Star-2 Bus	28790	125° W	WEST 15°
18	AMC-1 (GE-1)	A2100A	24315	128.6 W	WEST 18.6°
19	Ciel-2	Spacebus 4000 C4 (LARGEST BUILT)	33453	128.8 W	WEST 18.8°
20	GOES-15	BSS 601	36411	135 W	WEST 25°

The data was processed using a coded pipeline built in MATLAB. The first step of any astronomical observation is calibration of the data. Calibrations for each frame were taken separately in the form of twilight flat fields, on-sky darks, and bias images. Sky darks were taken directly after each science timeseries so that the sky background matched closely with that of the data. Most of the data sets were analyzed using these sky darks. An alternate method to remove sky noise was to instead use the dark portion of each individual image. By taking this dark area and subtracting it from each frame in the series individually, changes in the sky background which occurred on a timescale shorter than that which the data series covered could be removed. Each data image was then calibrated according to *EQUATION 4.1*.

$$\text{EQUATION 4.1} \quad \text{Calibrated Data} = \frac{\text{Science Image} - \text{sky Dark}}{\text{Flat}}$$

Once calibrated, each timeseries was run through an aperture summation program. All light intensity within a certain radius around the satellite was summed for each image in the series. The radius of this aperture varied from 20 pixels to 50 pixels in order to contain all light from the satellites, but cut out as much of the residual sky background as possible. This produced two synchronized series of intensity values taken over time, one from each camera (See *Figure 4.1, left* for an example of two intensity values plotted against time).

These two time series of intensity values correspond to two streams of orthogonally polarized (s and p) light from the satellite. They could then be compared to each other in order to calculate the degree of linear polarization (DOLP) of the signal [See *EQUATION 4.2*]. In this equation  $I_s$  and  $I_p$  each represent the summed intensity count for each of the individual frames seen in both cameras. See *figure 4.1, right side* for an example of a DOLP signal.

$$\text{EQUATION 4.2} \quad DOLP = \frac{I_s - I_p}{I_s + I_p}$$

This DOLP could then be further analyzed using Fourier techniques. Three separate metrics are used here, the first of which is a power spectrum. A power spectrum of the DOLP can be used to reveal any periodic elements to the signal. Essentially a power spectrum is the square of a fast Fourier transform, and thus represents the amplitude squared of the fast fourier transform (fft). See Appendix 7.2 for the definition of power spectrum in MATLAB. Peaks in the power spectrum should thus correspond to movements of the satellite.

Next, a spectrogram can be created from the DOLP (see Appendix 7.2 for the MATLAB definition of Spectrogram). This is essentially a Fourier transform of the original input (DOLP) plotted against time. These spectrograms are frequently used to analyze and clean audio signals, but are used here to recognize features that might allow us to distinguish signals taken from different satellites.

Finally, a spectral kurtosis of the DOLP can be analyzed. The math behind this technique can be found in Vrabie et. al. and Nader et. al. [10][8]. According to Nader et. al.[8], it can essentially be described as:

*“The kurtosis is a statistical parameter based on the fourth moment of a signal, which is close to zero for gaussian noise and other stationary signals, but large for impulsive signals containing series of short transients, such as a bearing fault signal.”*

Although they are using kurtosis to describe bearing faults in a signal, the theory remains relevant for use in analysis of the HTI DOLP signal. Vrabie et al. [10] further describe the process by which spectral kurtosis can be used to verify spectral lines (frequencies) in a time series signal. Both authors use a spectral kurtosis in conjunction with a power spectral density calculation in order to pull out useful frequencies.

By looking at these three metrics (power spectrum, spectrogram, and spectral kurtosis), frequencies can be pulled from each DOLP signal which should correspond to satellite motions.

## 4.2 Comparison of Several Target Satellites and Stars

As stated previously, the project was given two nights of telescope time on the 61" Kuiper telescope in each of May, July, August, September, October, and December. During the May run, the Grasshopper detectors were used and as such this data was not ideal. It did not contain enough signal in order to be useful, so it will not be shown here. After this, the Andor Zyla detectors were used during the rest of the nights. Cloudy weather in July prevented us from taking useful data, however August, September, and October nights proved to be useful.

Data from the August, September, and October runs has been analyzed according to the above procedure and is presented here. Much of the data which was taken is not mentioned here. The most interesting sets of data have been analyzed in the sections below.

### 4.2.1 Satellite Ciel-2 [NORAD ID: 33453]

Several sets of data were collected for Ciel-2 over the September and October nights. Shown immediately below (*figure 4.1*) are intensity and DOLP graphs of one set of data taken on September 26. This data set is notable because it was captured as the intensity appeared to be becoming much brighter over time. Although an overall change in intensity should not affect the DOLP, it's clear that there is roughly a change of ~13.5% in the DOLP as the signal intensifies over 645 seconds (*Figure 4.1*).

This change in DOLP and brightness can be accounted for by the fact that this particular data set was taken near twilight. In fact, what is being seen is the increase in overall sky brightness as sunrise approaches. This can be removed by subtracting off dark sky values from each individual frame rather than by subtracting a single set of darks which were taken directly after the data set (as was done in all other data seen here).

In order to further analyze the signal, it was broken into pieces surrounding the stray star spikes. This was done in order to remove the noise in the power spectrum and spectrograms which is created by the stray stars.

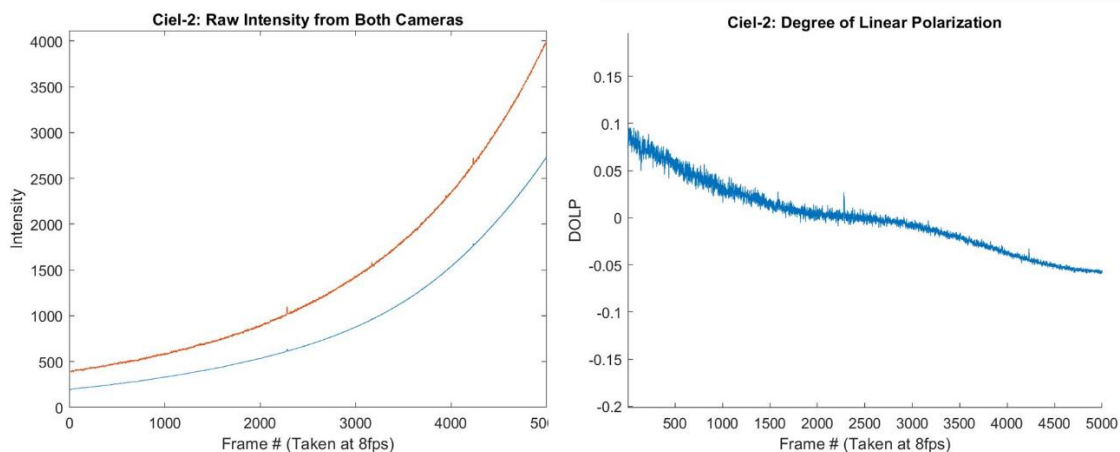
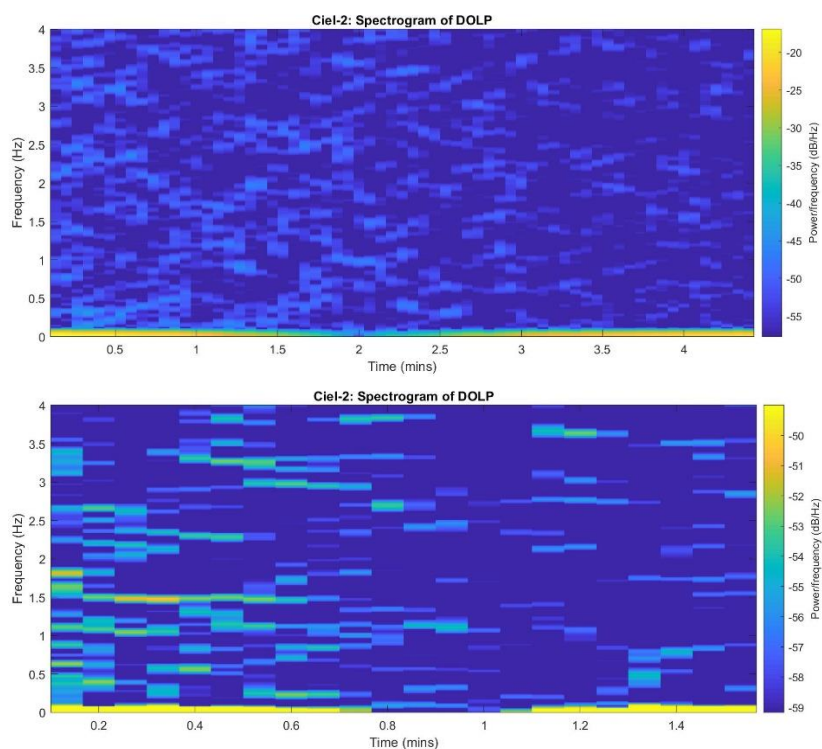


Figure 4.1: Full length Intensity and DOLP September 26. There are several stray stars which drifted through the aperture, which can be seen as spikes in the intensity and DOLP. This set of data was taken at a rate of 8fps over a 256x256 region of interest on the detector.



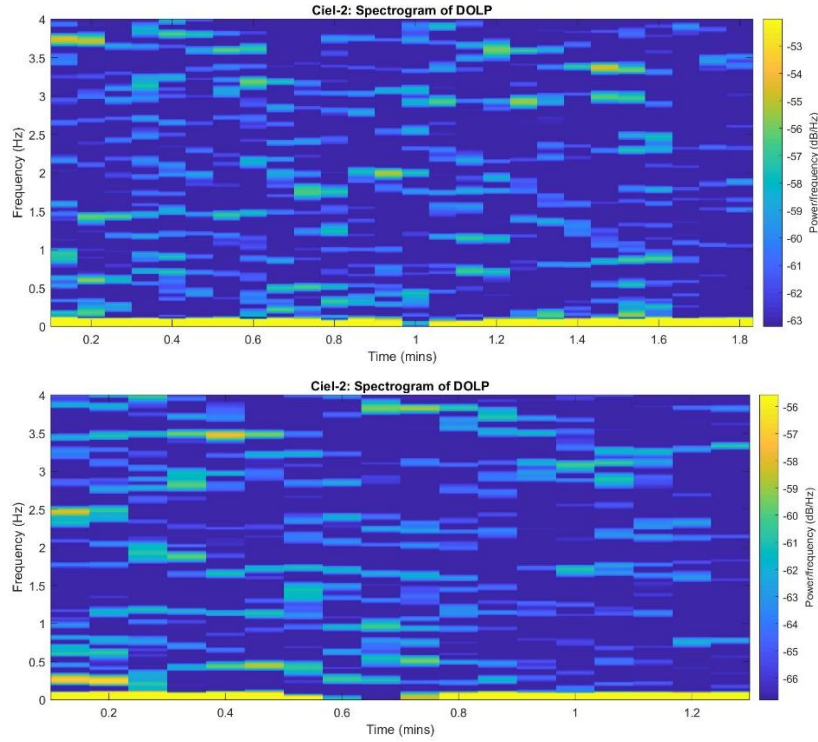


Figure 4.2: Spectrograms of each part of the above signal. Top: part 1, Bottom: part 4. Data taken at 8fps.

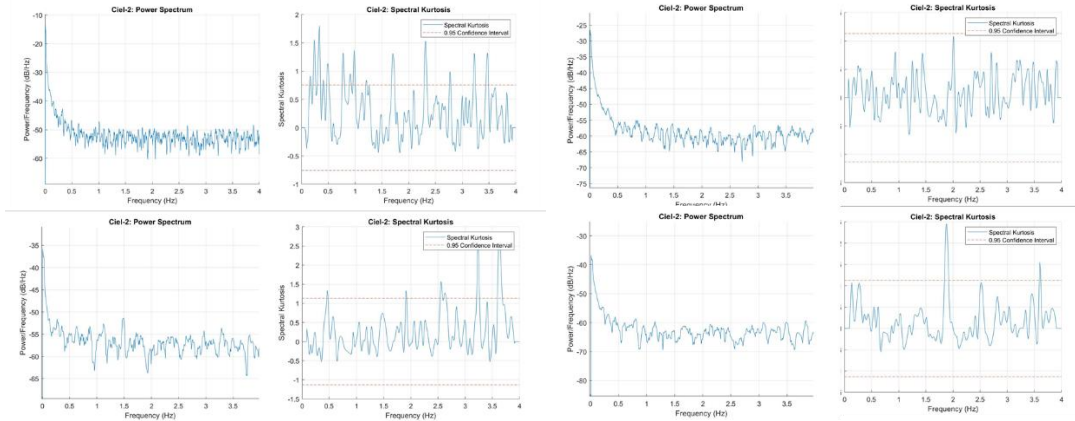


Figure 4.3: Power spectra and spectral kurtosis of each of the four parts taken at 8fps. Top Left: part 1. Bottom Left: part 2. Top Right: part 3. Bottom Right: part 4.

From these power spectra it would appear that there are common peaks at 0.08Hz in all parts of the signal. However this is not visible in the spectral kurtosis and may only be a false peak due to noise.

Another set of data taken on September 26, taken at 20 fps over a 256x256 region, show much different signal. The DOLP, power spectrum, and spectrogram below show this second set of data (figures 4.4, 4.5, 4.6).

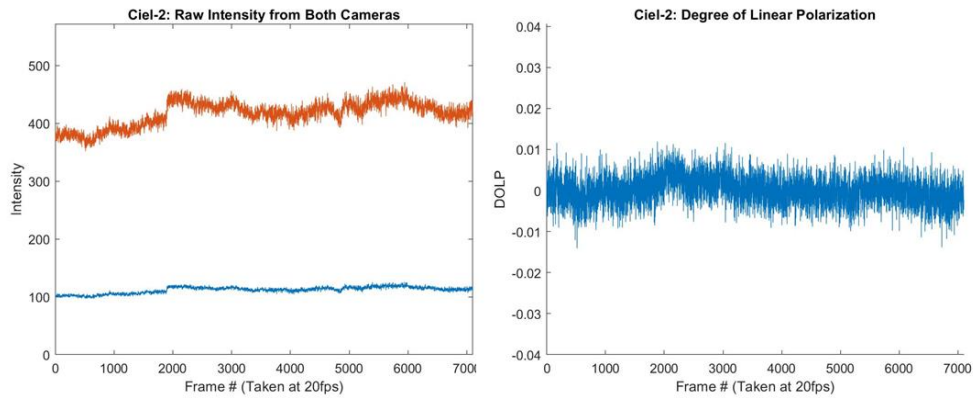


Figure 4.4: Intensity and DOLP of Ciel-2, September 26. This set of data was taken at a rate of 20 fps.

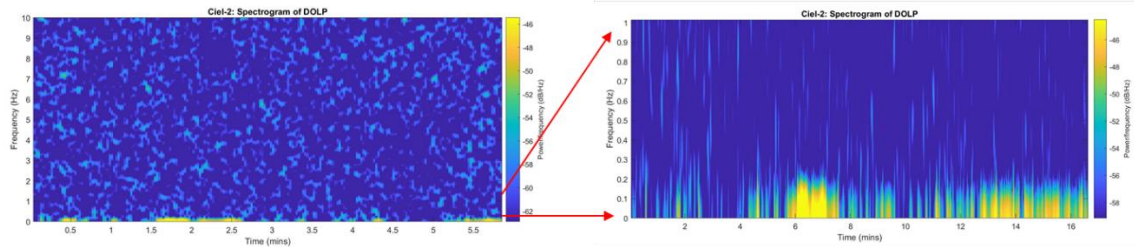


Figure 4.5: Spectrogram of the DOLP for the above signal taken at 20fps. Left: full signal. Right: The vertical axis only extends to 1Hz.

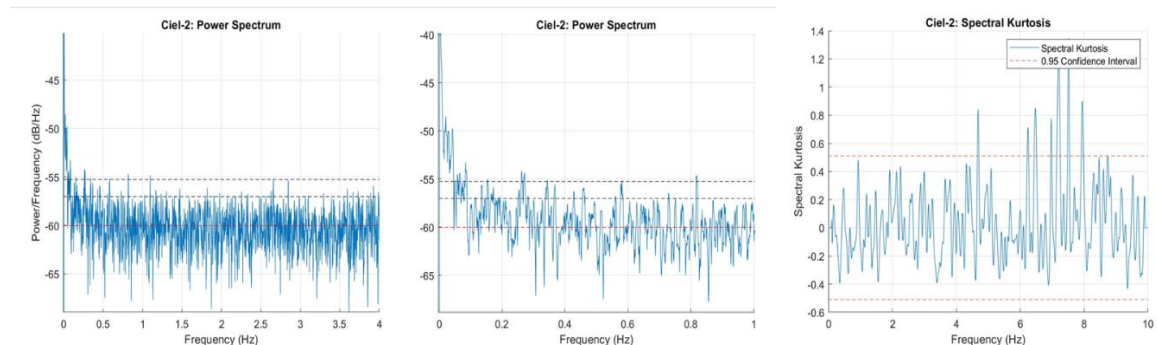


Figure 4.6: power spectra and spectral kurtosis of the signal taken at 20fps. Left: full power spectrum, Center: power spectrum for low frequencies only, Right: Full spectral kurtosis.

From the DOLP and the Spectrogram, it appears that there is an artifact present in the signal of this satellite. Peaks of 0.028, 0.043, 0.08, 0.26Hz can be pulled from the power spectrum. It is possible that this signal is due to some satellite maneuver.



#### 4.2.2 Satellite StarOne/Brasilsat B4 [NORAD ID: 26469]

This object is particularly interesting as it is a spin stabilized satellite. The rotation period is known to be roughly 1.08 rotations per second [4]. Because it is in constant rotational motion, analysis of this data set shows a constant, periodic signal over the entire length of the timeseries (where other objects seem only to show unique signals when they are in the process of maneuvering).

Data for this object was taken over three nights: 9/25/18, 9/26/18, and 10/21/18. It was taken with a region of interest of 256x256 pixels in each case and shows periodic movements throughout the entire signal. Shown below, *Figure 4.7* represents the DOLP calculated from the simultaneous intensity measurements in each channel (s and p). Figure 4.8 then shows several spectrograms of these DOLP signals. Finally, *figures 4.9a and 4.9b* show a power spectrum and spectral kurtosis of each signal.

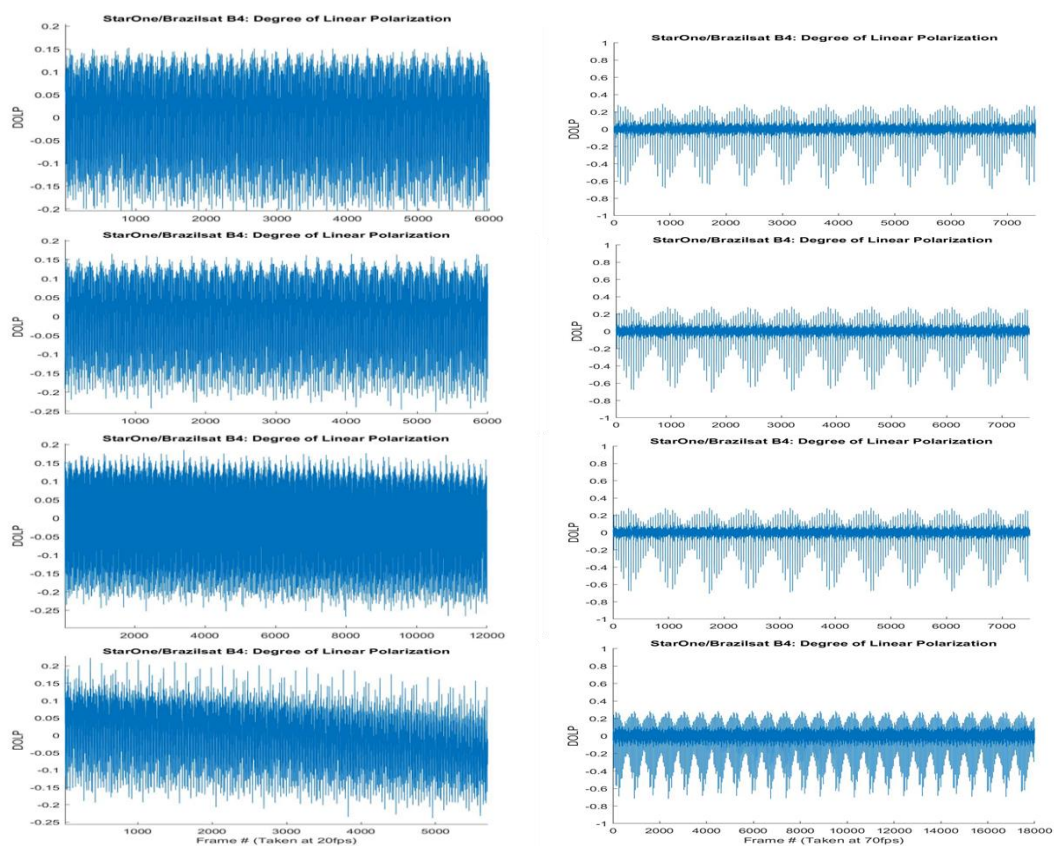


*Figure 4.7: Comparison DOLP over the September nights. Shown here is the full signal length. Left: September 25 Data. Right: September 26 Data. Note: The scaling on the y-axis is a bit different between the two nights.*

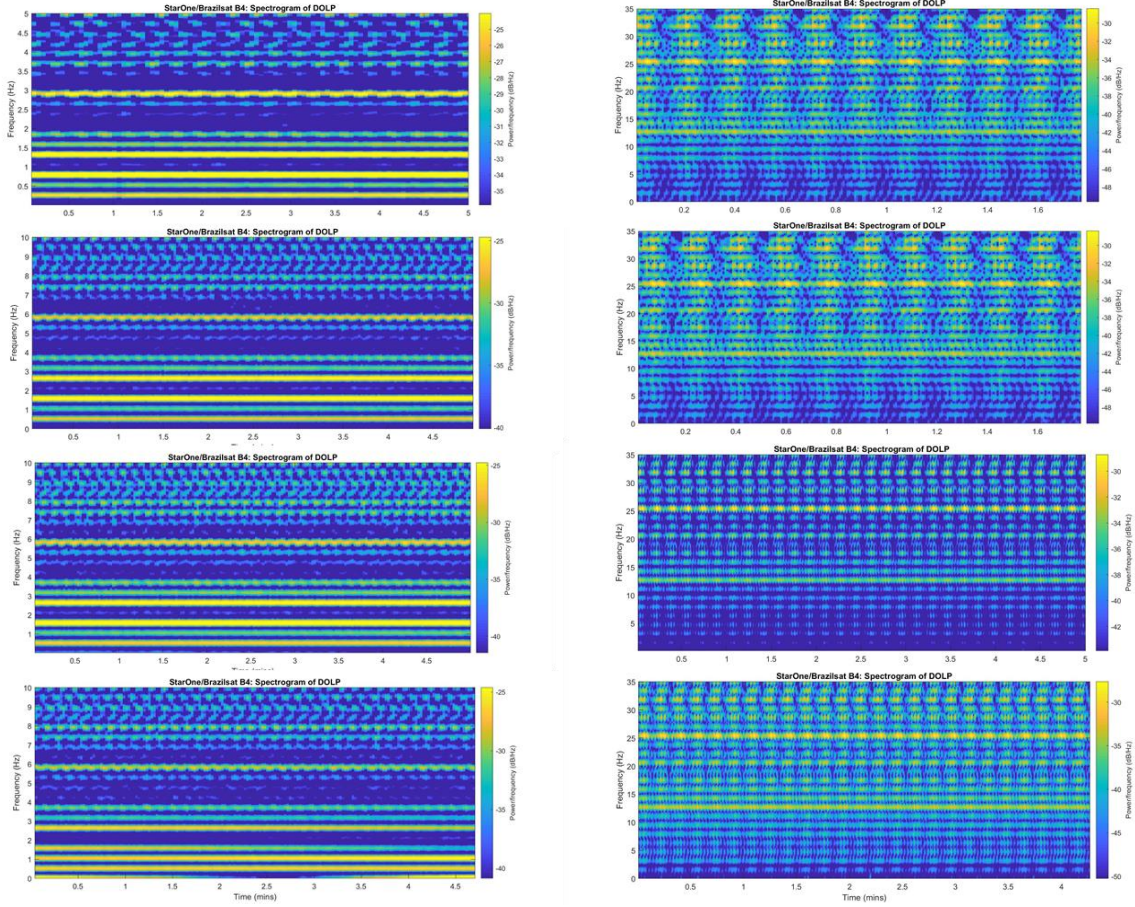


Figure 4.8: Spectrograms of the above DOLP for four sets of signals on two nights. These spectrograms have been cut to 5 minute lengths (with the exception of the top right two, where total lengths are given). Left: September 25 data. Right: September 26 data.

Further analysis of the power spectrum and spectral kurtosis shows that the signals for the two September nights have consistent peaks (at least) at: 0.53Hz, 1.06Hz, 1.59Hz, 2.1Hz, 2.65Hz, 3.18Hz, and 3.71Hz. This appears to be roughly consistent with the known rotation period of the HS-376 bus, which was measured to be  $\sim 1.08$  seconds in 1987 [4]. Table 4.2 shows the calculated peaks in the power spectra of each of the observations.

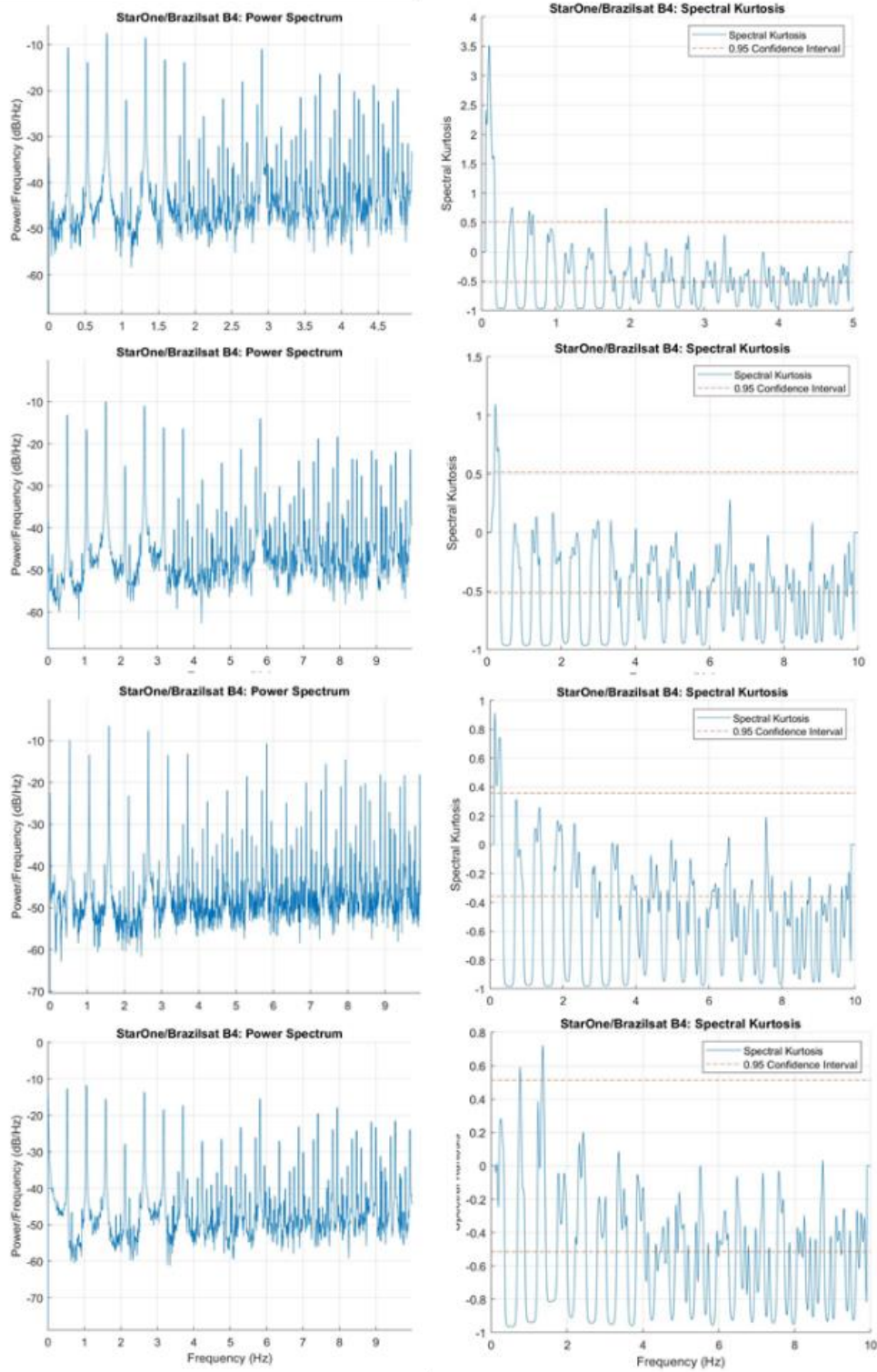


Figure 4.9a: Power spectrum and spectral kurtosis of each of the September 25 data sets. The spectral kurtosis serves as a sort of check to be sure that the power spectrum peaks are real.



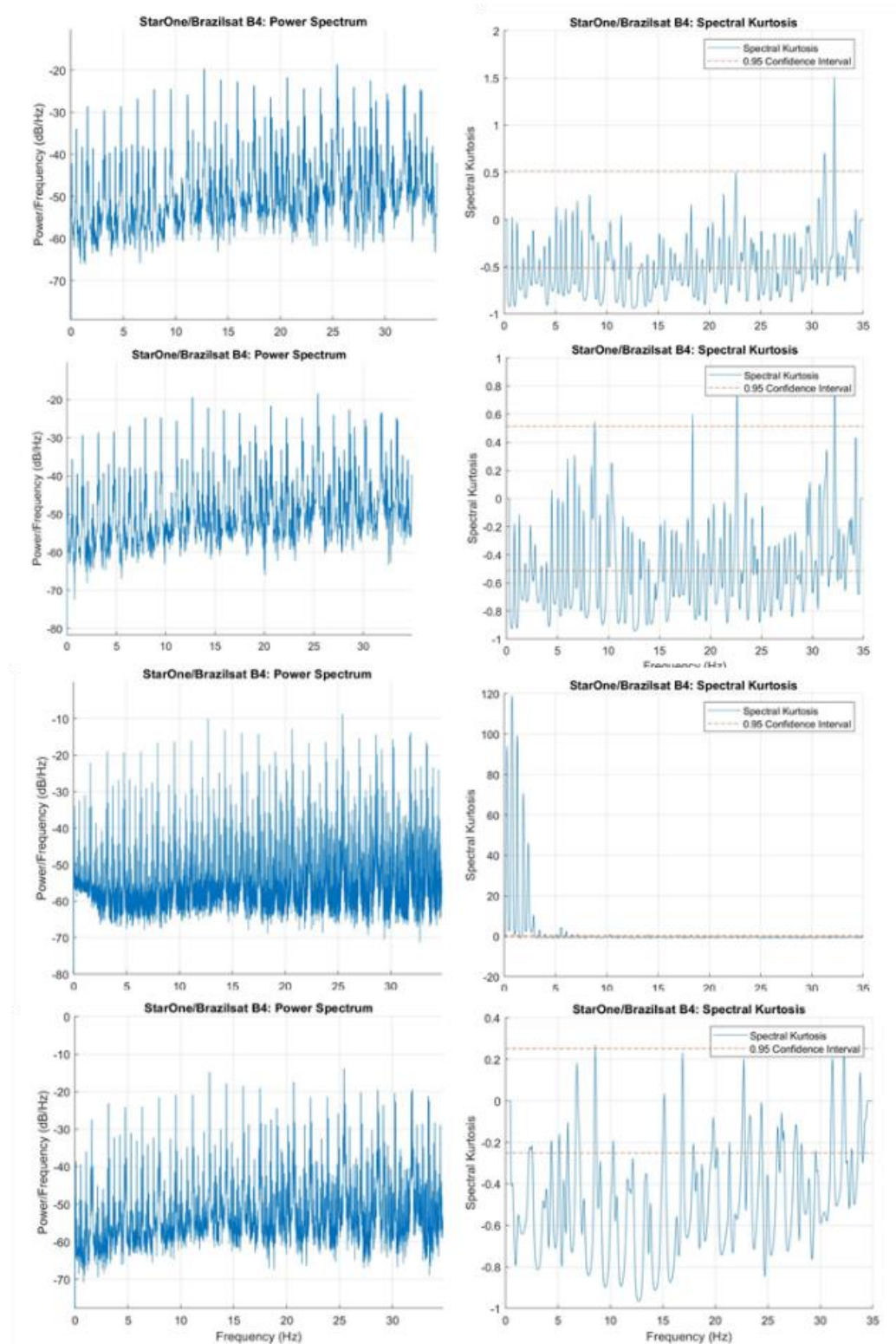


Figure 4.9b: Power spectrum and spectral kurtosis of each of the September 26 data sets.

Giles et al. [4] suggest that these GEO satellites should be brightest near the equinox, which was on September 22, 2018. Indeed, it was seen that this particular satellite was very bright

during the September observations, and thus a signal to noise ratio of at least  $\sim 15$  in each frame was easily acquired for these two nights, even when taking data at a high rate of 70fps. However, during the October night the satellite was much fainter. Therefore, it was taken at a much slower rate (only 4fps as compared to the 70fps which was possible in September). Even with the longer exposure times, each image was only acquired with a signal to noise ratio of  $\sim 2.5$ .

Because of this low signal, the final set of data was much more difficult to analyze. *Figure 4.10* shows the spectrogram of the October data and *figure 4.11* gives the power spectrum and spectral kurtosis. Using the spectral kurtosis only, peaks of 0.58Hz, 1.02Hz, and 1.48Hz were found.

It should be noted that the error in these peaks is much greater for two reasons. The first being the poor signal of the data, and the second being the spectral kurtosis method of analysis in itself. Spectral kurtosis analysis works best when there is a power spectrum to compare to [10][8]. However in this case, there was too much noise in the power spectrum to prove useful, so only the kurtosis was analyzed for its peaks. *Figure 4.11* shows a comparison between the power spectrum and the spectral kurtosis of the October data.

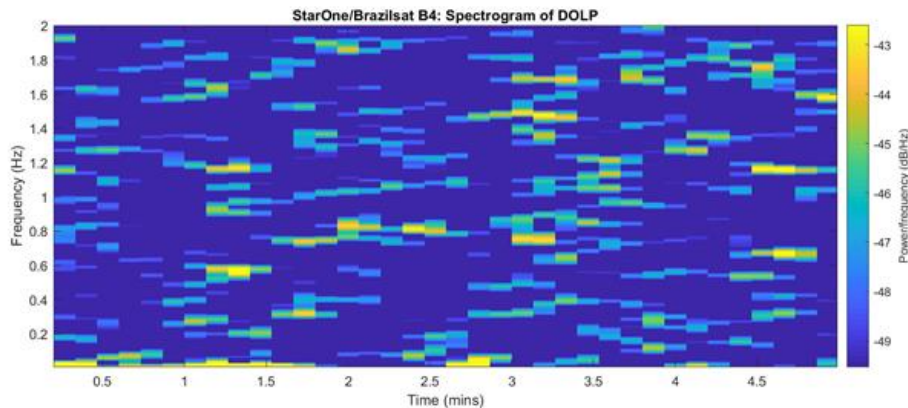


*Figure 4.10: Spectrogram of DOLP for October 21 data set.*

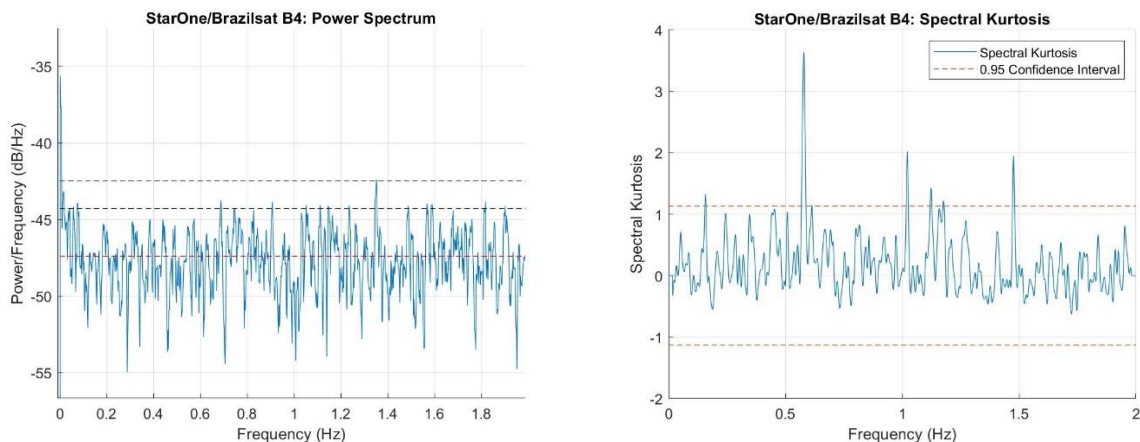


Figure 4.11: Left: Power spectrum of October 21 data. Right: Spectral Kurtosis.

Table 4.2: Calculated peaks in the Power Spectrum of each set of observation data taken over all three nights.

Peaks in Power Spectrum [Hz]															Frame Rate [fps]
26-Sep															
set2	0.105	0.532		1.064		1.589		2.114		2.646		3.185		3.71	70
set3	0.09954	0.5298		1.06		1.589		2.119		2.646		3.179		3.709	70
set4	0.09954	0.5298		1.06		1.589		2.119		2.646		3.179		3.709	70
set5	0.09954	0.5298		1.06		1.589		2.119		2.646		3.179		3.709	70
set6	0.09954	0.5298		1.06		1.589		2.119		2.646		3.179		3.709	70
25-Sep															
set2	0.265	0.53	0.795	1.058	1.323	1.588	1.853	2.118	2.383	2.65	2.913	3.177	3.442	3.707	10
set3		0.53		1.06		1.59		2.12		2.647		3.177		3.707	20
set4		0.53		1.058		1.588		2.118		2.648		3.177		3.707	20
set5		0.5298		1.06		1.589		2.116		2.649		3.179		3.705	20
21-Oct From Spectral Kurtosis															
run1		0.578		1.022		1.476									4

These data have been taken over three separate nights. Thus it would seem to show that a particular signal can be associated with StarOne/Brasilsat B4 over at least one month's time. It would also seem to show that despite the poor signal in the October data, at least some of the rotational frequencies could still be found.

#### 4.2.3 Satellite DirecTV-15 [NORAD ID: 40663]

Data was taken over several nights, however the most interesting set was taken on September 26. The detector region of interest was set to 256x256 pixels, and it was a clear night. This data is shown below.

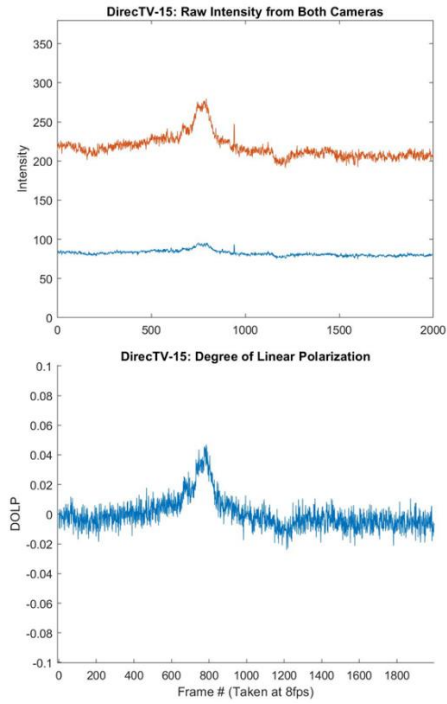


Figure 4.12: September 26 data. Top: Intensity of each channel. Bottom: DOLP

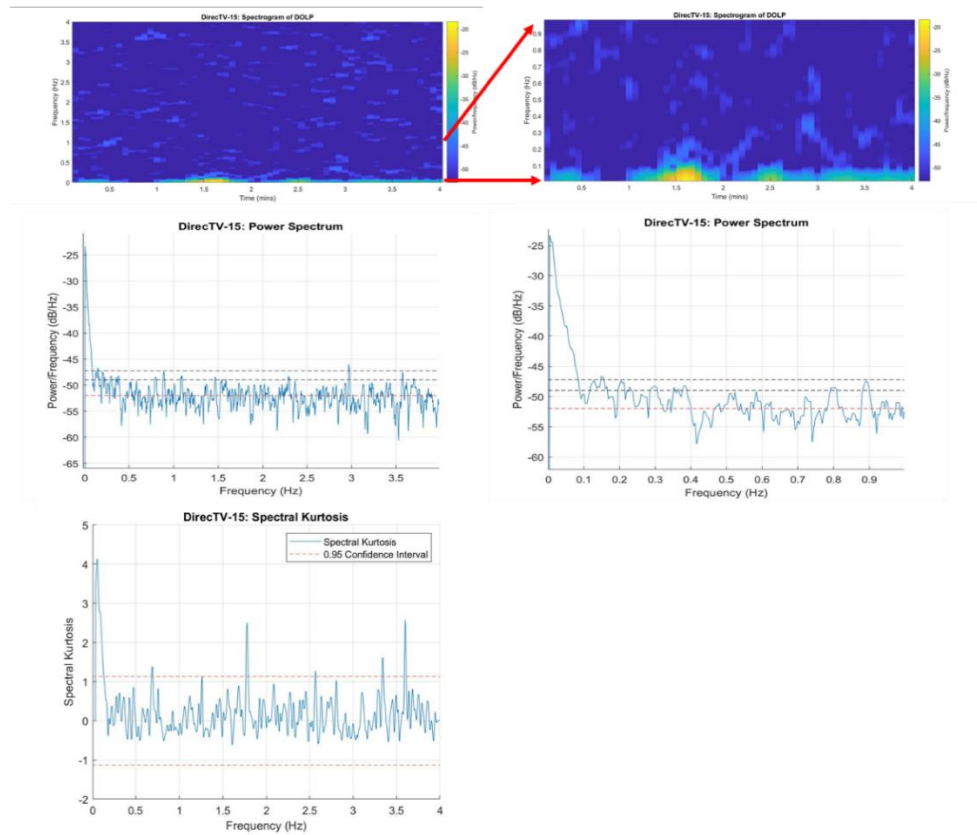


Figure 4.13: September 26 data. Spectrogram, Power Spectrum, Spectral Kurtosis.

After reviewing the DOLP and spectrogram it would appear that there is an artifact present in the signal of this particular satellite, beginning near frame  $\sim 600$  and ending at  $\sim 800$ . Since data was taken at 8fps, this corresponds to roughly 3 minutes in length. Upon further analysis of the power spectrum and the spectral kurtosis they appear to both have significant peaks at 0.069Hz and  $\sim 0.05\text{Hz}$  (0.052 and 0.056 Hz respectively). This could indicate the presence of a satellite maneuver taking place.

#### 4.2.4 Stars as Comparison

For comparison, data was also taken on several stars. It is expected that these stars will exhibit no unique signatures in DOLP. One of these stars is shown below.

##### TYC 2267-506

Shown below are several figures representing data taken on September 26, 2018. Looking at the intensity values of the signal (top left in *Figure 4.14*), at first glance it would appear that there are some variations in the star's intensity over time. However, since the DOLP shows a relatively flat signal over time, this would suggest that these variations are due to atmospheric effects such as a change in atmospheric transparency or scintillation. However, the important thing to note is that there do not appear to be any significant changes to the relative s and p polarizations over time. Plotting a spectrogram and the power spectrum (right side of *figure 4.14*) of this signal would seem to show consistency with this conclusion.

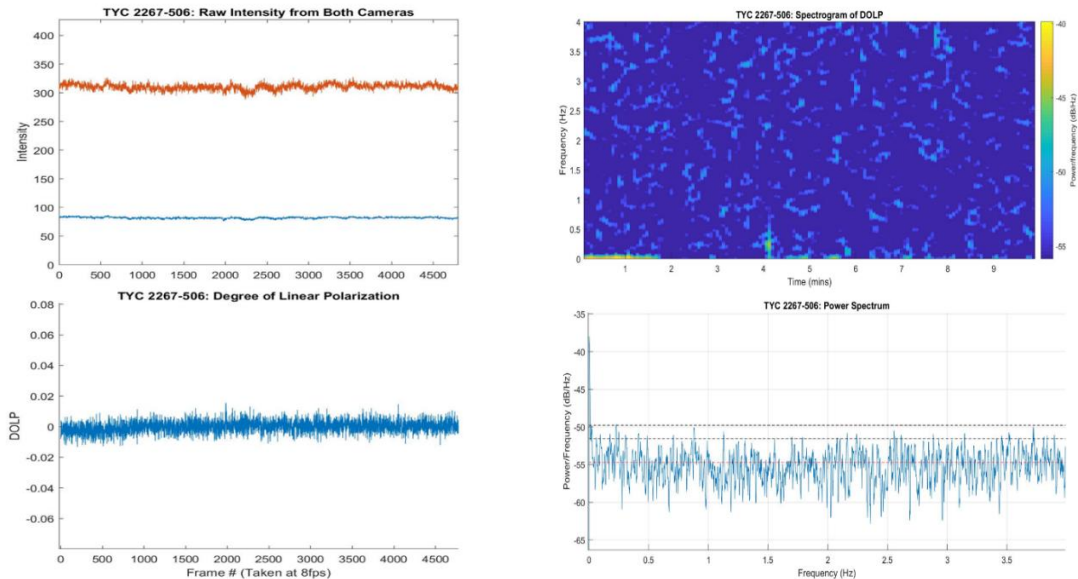


*Figure 4.14: Left: Raw intensity and DOLP for TYC 2267-506. Right: Spectrogram and Power Spectrum of the star. Black dotted lines on the power spectrum represent the first and second standard deviations of the signal, while the red dotted line represents its mean.*



A closer look at the power spectrum reveals that there are two very low frequency peaks which rise above two standard deviations located at: 0.001667Hz and 0.003333Hz. It would seem that these correspond to errors in the calculation of the discrete fourier transform, which arise from edge effects of the signal (see Appendix 7.1, 'periodogram()' for a description of the MATLAB function). Therefore it can be said that this signal is sufficiently flat and featureless, and suggests that at least this star does not exhibit the same signals seen in GEO satellites.

### 4.3 Comparison of Signal with Telescope Tracking On and Off

#### DirecTV-15

In order to satisfy the third goal of the observations (that is to determine whether the telescope tracking affects signal in the data), data was taken first with telescope tracking turned on, then with tracking turned off. The two series in *figure 4.15* were taken at 7fps, over a time of ~142 seconds. The region of interest was cropped to 128x128 pixels on the detector (only this area was read out).

During the course of this set of data, the telescope tracking 'bumped' the image several times. Each bump resulted in an initial offset of approximately 10 pixels, followed by several smaller periodic movements as the position equalized. The smaller periodic movements appear to take place over much shorter time periods (~1 second), with their amplitude and frequency decreasing as time progresses. These secondary movements appear to show up with some regularity in a spectrogram of the DOLP (*figure 4.15, left*).

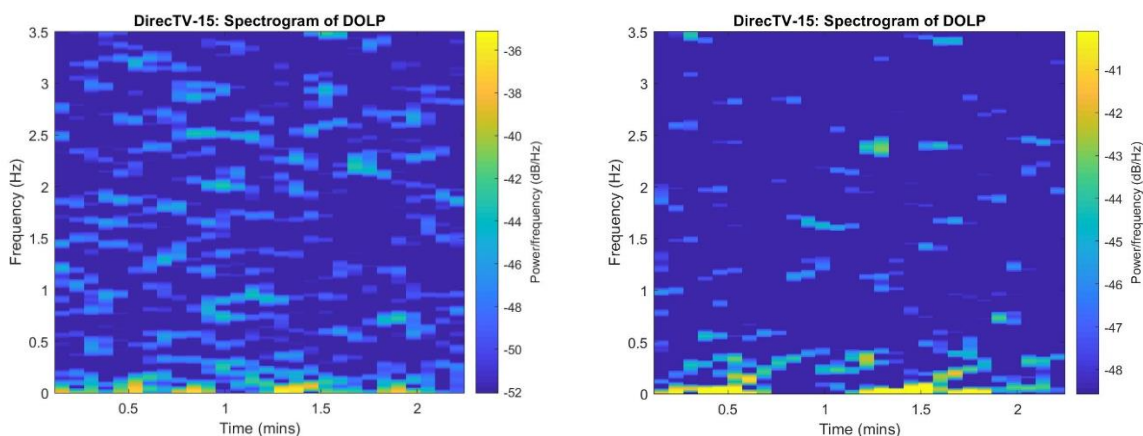


*Figure 4.15: Spectrogram of DirecTV taken at 7fps on August 21. Left: Tracking ON. Right: Tracking OFF.*

Although in theory these effects due to tracking can be removed, it seems a much easier approach to simply take data with the telescope tracking turned off.

#### 4.4 Noise in the Signal: Clouds vs Signal

Part of the power of the HTI instrument comes when clouds are present or in any case of varying signal intensity. Since HTI measures a relative change in degree of linear polarization, only changes in the s or p polarized signal will register as a signal. However, overall changes in intensity (such as might happen as the satellite crosses opposition and fades out) should not register a change in DOLP. *Figure 4.16* shows an example of overall intensity change over time compared to the DOLP signal.

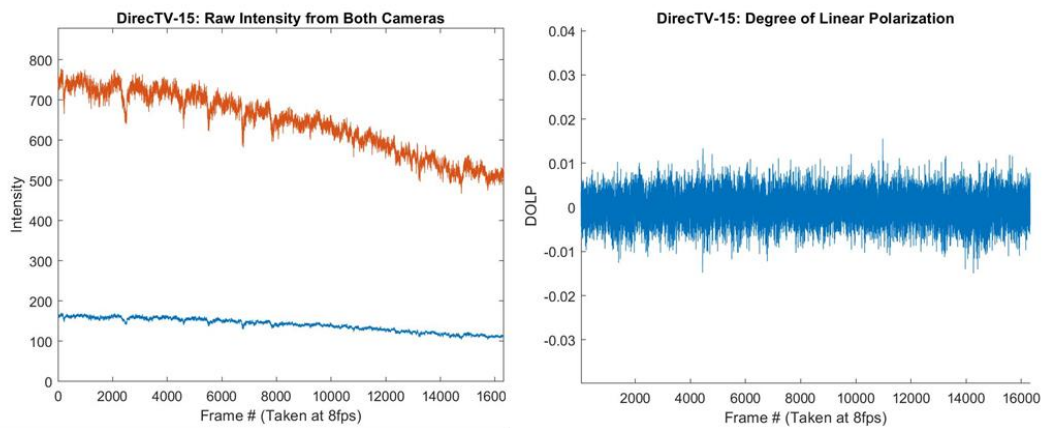


*Figure 4.16: Data from October 21, taken at 8fps on DirecTV-15. The above signal shows a long, overall change in intensity as the satellite moves past opposition to the sun. Note even as the individual intensities change quite a bit the DOLP signal remains very flat.*

In the case of clouds, a difference in DOLP can actually be registered. However it is not hard to distinguish this false DOLP signal from a real signal. First, clouds will always result in a drop in intensity, whereas satellite signals can actually increase in intensity as they move. Second, the overall change in signal intensity due to satellite maneuver will be relatively small (on the order of ~20% intensity change). Clouds on the other hand, can result in far greater changes in the intensity levels. And lastly, the change in intensity when clouds are present is very fast. Within only 1 or 2 frames, an intensity drop of 50% or more can be seen. Satellite movements tend to take place over a few minutes and are less dramatic.

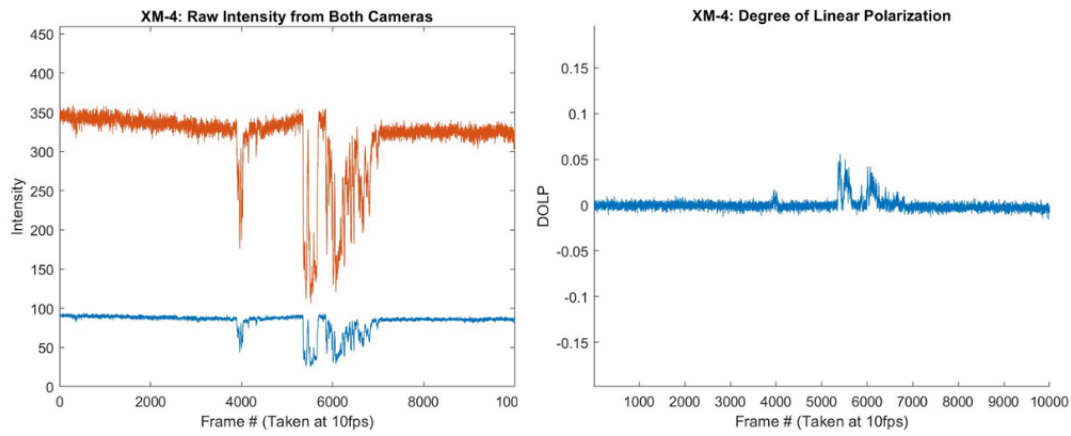


Figure 4.17: The above signal on October 21 on satellite XM-4 was taken at 10 fps as clouds moved through the field of view. The instantaneous drop in intensity is roughly 65%.

## 5 Results and Discussion

Overall, the newly upgraded HTI instrument performed to its design specifications. Several GEO satellites were observed throughout the course of several months. Their polarization signals were then analyzed using the Fourier techniques (power spectra, spectrograms, and spectral kurtosis) outlined in section 4.

### 5.1 Performance of the HTI Instrument Upgrade

The newest instrument performed as modeled. Evidence of this performance can be seen in the data which was collected over 10 nights during the past few months. Optical aberrations were never the limiting factor, instead natural seeing and atmospheric effects limited the resolution of the system. Imperfections in the system such as dust blots and intensity variations in the system due to vignetting were calibrated out using twilight flats and darks with no further troubles. Vignetting in the system did not cause problems, as most of the data taken was over a much smaller field of view (smaller regions of interest were used on the detectors in order to speed up the readout times).

The larger field of view did however serve another purpose. It made finding each object much easier and quicker. The Kuiper telescope pulls TLE tracking files from an unknown online source. As a result of this, some of the tracking files were not very accurate. With the large FOV finding some of these targets became much easier. In addition, it allowed for the tracking of various objects not discussed in this analysis. Telescope tracking could be turned off while a moving object was allowed to drift through the field.

## 5.2 Result of Comparison of Several targets (Observational Results)

Clear signals could be found in at least three different satellites. Each of these stands out as distinctly different from a background star (TYC 2267-506) as well as from any noise due to clouds overhead.

### **StarOne/Brasilsat B4 [NORAD ID: 26469]**

This satellite is an HS-376W bus, which is a spin stabilized satellite. Instead of the usual solar panel wings, its cylindrical body is plated in solar panels [4].

In the case of StarOne/Brasilsat B4, very clear peaks in the power spectrum and spectral kurtosis of the September data indicate frequencies of 0.53Hz, 1.06Hz, 1.59Hz, 2.1Hz, 2.65Hz, 3.18Hz, and 3.71Hz. Although the October data had a lower signal to noise ratio ( $\sim 2.5$  rather than the  $\sim 15$  from the September data), peaks of 0.58Hz, 1.02Hz, and 1.48Hz were still found present in the signal. These were found by analyzing a spectral kurtosis of the signal. If the October data can be trusted, then this is interesting as it indicates that even with very faint satellites, the HTI instrument has the capability to find useful signals and identify satellites. The above frequencies appear to be consistent with the known HS-376 rotation period of  $\sim 1.08$ s [4].

### **Ciel-2 [NORAD ID: 33453]**

Ciel-2 is a Spacebus-4000C4 bus, which is the largest of its kind. It is very similar in shape to the Eurostar-3000 bus, except that the solar panels are much larger [19].

Two sets of data have been analyzed here. The first set of data shows a signal taken over a  $\sim 10$  minute period of time in which the satellite intensity is increasing consistently. The DOLP also shows a somewhat constant decrease over this long period of time (a total change of  $\sim 13.5\%$  from start to finish can be seen). This indicates that the polarization signature is changing from slightly s-polarized to slightly p-polarized as the overall intensity increases. This overall shift in DOLP over the length of the signal can be attributed to the brightening of the background sky as sunrise approached. In addition, all parts of the signal there are frequency spikes present in the power spectrum at 0.08Hz.

The second set of data appears to show two changes in the DOLP over a much shorter timescale (each take place over 1-2minutes). Peaks of 0.028, 0.043, 0.08, 0.26Hz can be pulled from the power spectrum of the signal. This could indicate a satellite maneuver is taking place during this time period, however more satellite modelling is needed to confirm this.

## **DirecTV-15 [NORAD ID: 40663]**

This satellite is a Eurostar-3000 bus [18], which consists of a small body with two solar panel wings.

One set of observational data has been analyzed above. The DOLP and spectrogram of this particular set would seem to show a satellite maneuver is taking place. Analysis of the power spectrum and the spectral kurtosis shows significant peaks at 0.069Hz and ~0.05Hz (0.052 and 0.056 Hz respectively).

Additionally, data from this satellite was used as a test to determine if telescope tracking errors were present as artifacts in the data streams. It was determined that although frequencies created by the telescope tracking could in theory be removed during the analysis, it was easier to simply take any future data without the use of tracking.

### **5.3 Discussion**

During the observation runs, problems with the Andor Zyla cameras overheating were frequently seen. After taking longer sets of data, it was often necessary to stop, open up the instrument, turn off the cameras, and allow them to cool for a number of minutes before resuming observations. This problem could be solved in future runs with the use of water cooled models of the same cameras. The use of these detectors would also likely reduce the overall noise in the data due to the detectors. Therefore should more observations be done, a cooled camera system is recommended.

This HTI instrument has been designed for use on the 61" Kuiper telescope. However, there exists the possibility to adapt the instrument for use on the 90" Bok telescope, located on Kitt peak. This would of course allow for greater signal and could be a useful adaptation, especially when observing satellites which are not near opposition (and not near the equinox).

There has been a great deal of work suggesting that as satellites emerge from Earth's shadow (during an eclipse), the sudden temperature difference can create vibrations in the satellite solar panels. It may be possible for HTI to see these vibrations and learn something about that satellite. Observing one of these eclipsing satellites may be worth investigating in the future.

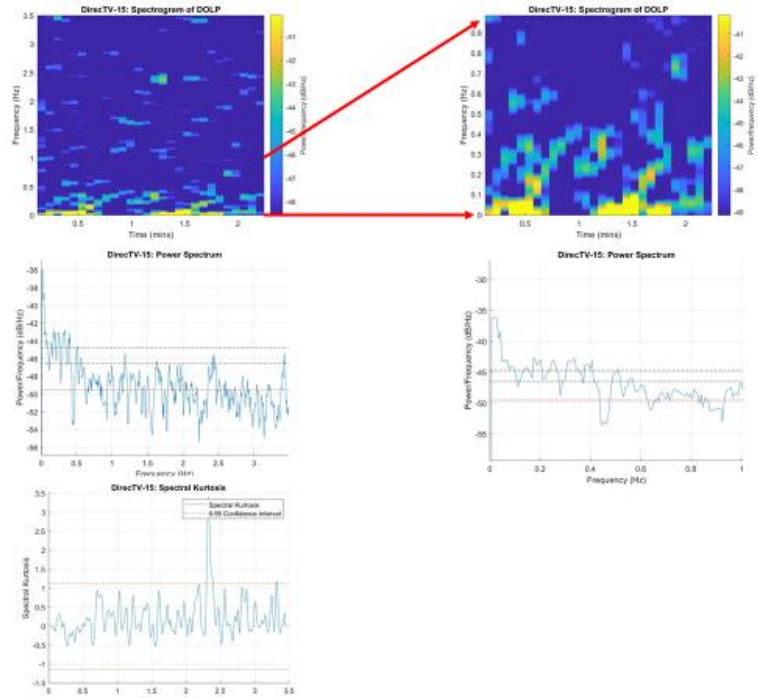
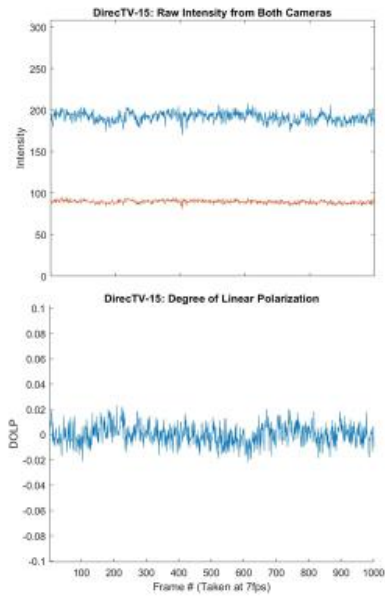
Lastly, as mentioned in the design section, there is some vignetting present in the current design. This was necessary to allow for the optomechanics to fit into the current frame of HTI. In future observations, it may be useful to re-work the optomechanics to allow for a larger M3/M4 configuration and thus reduce vignetting in the horizontal direction to zero.

# 6 Appendices

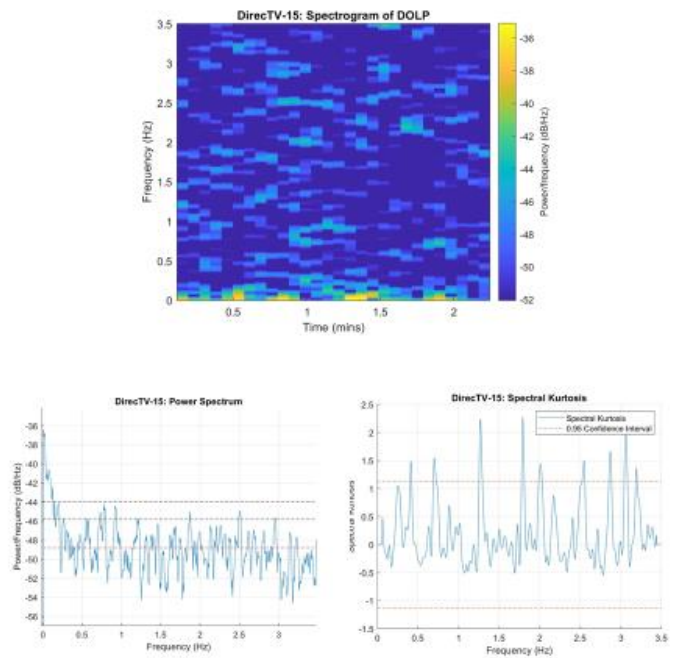
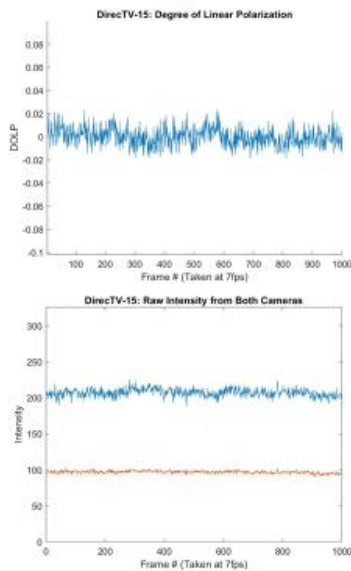
## 6.1 List of Data Figures

DirecTV-15 - NORAD ID: 40663

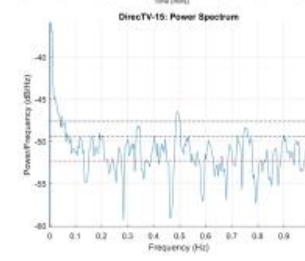
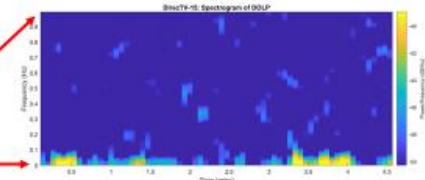
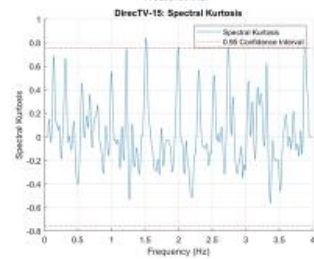
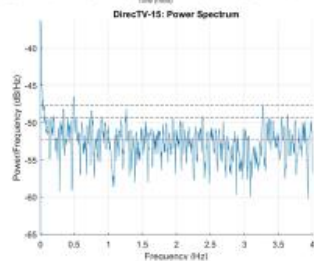
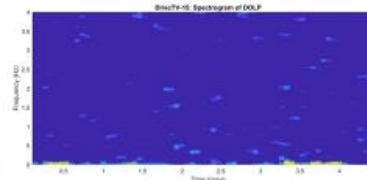
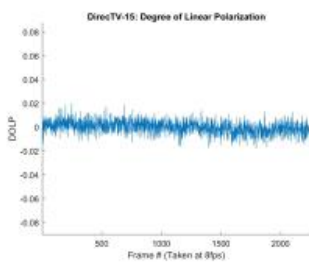
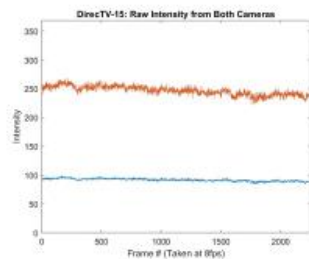
8/28/18



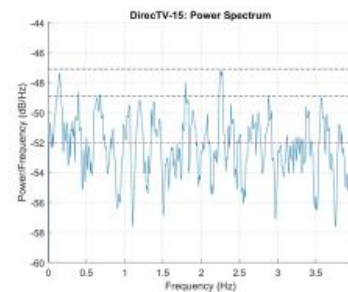
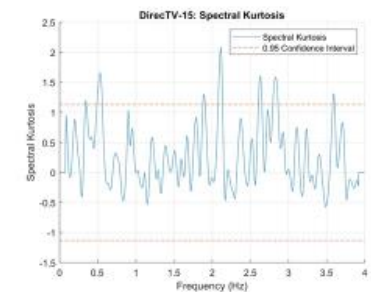
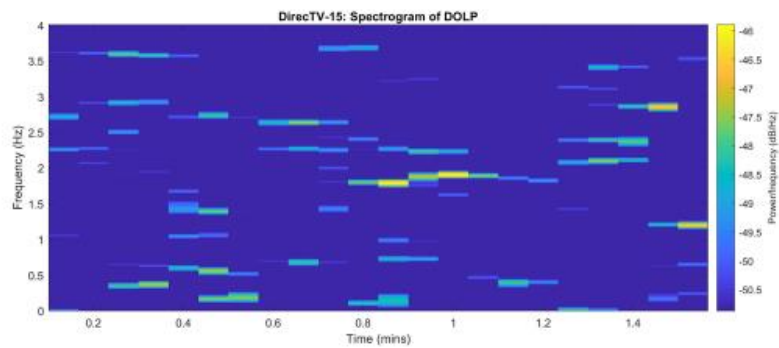
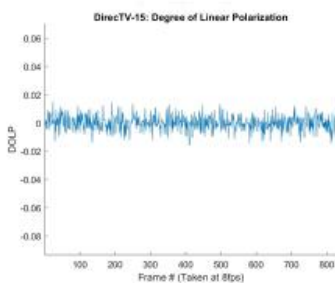
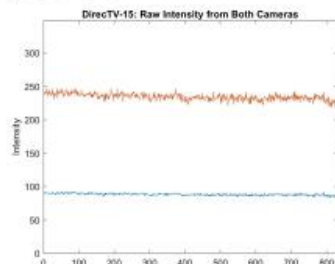
8/28/18,  
Tracking ON



9/26/18 run1  
part 2

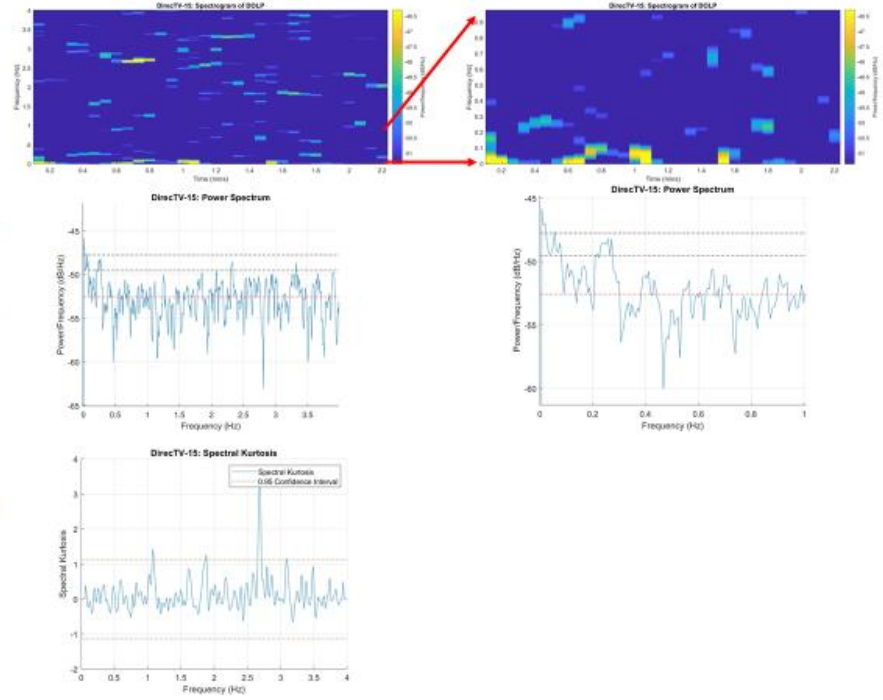
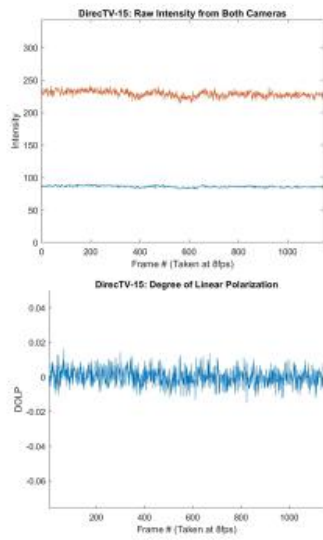


9/26/18 run1  
part 3

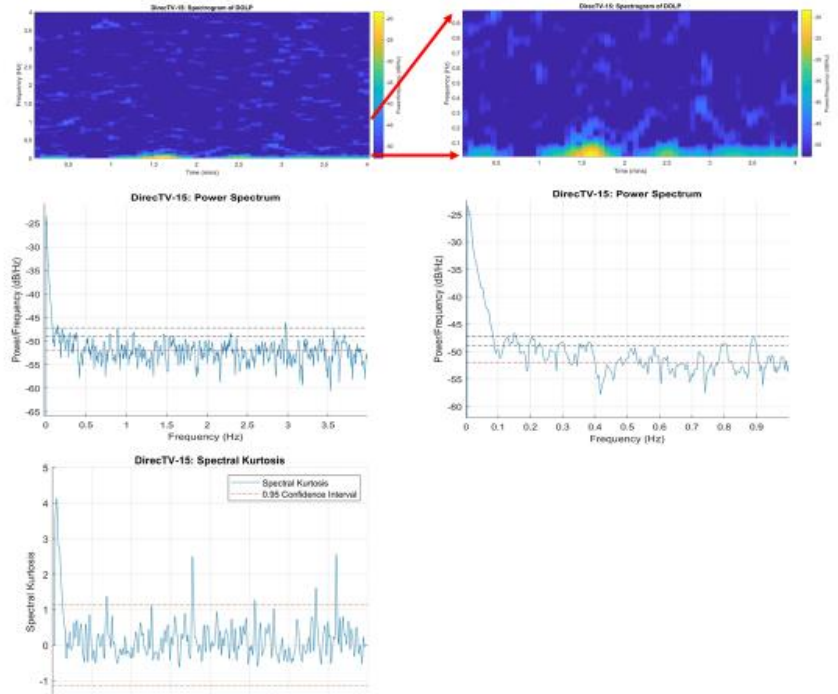
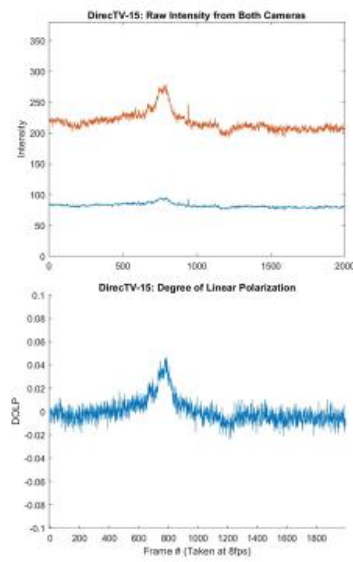




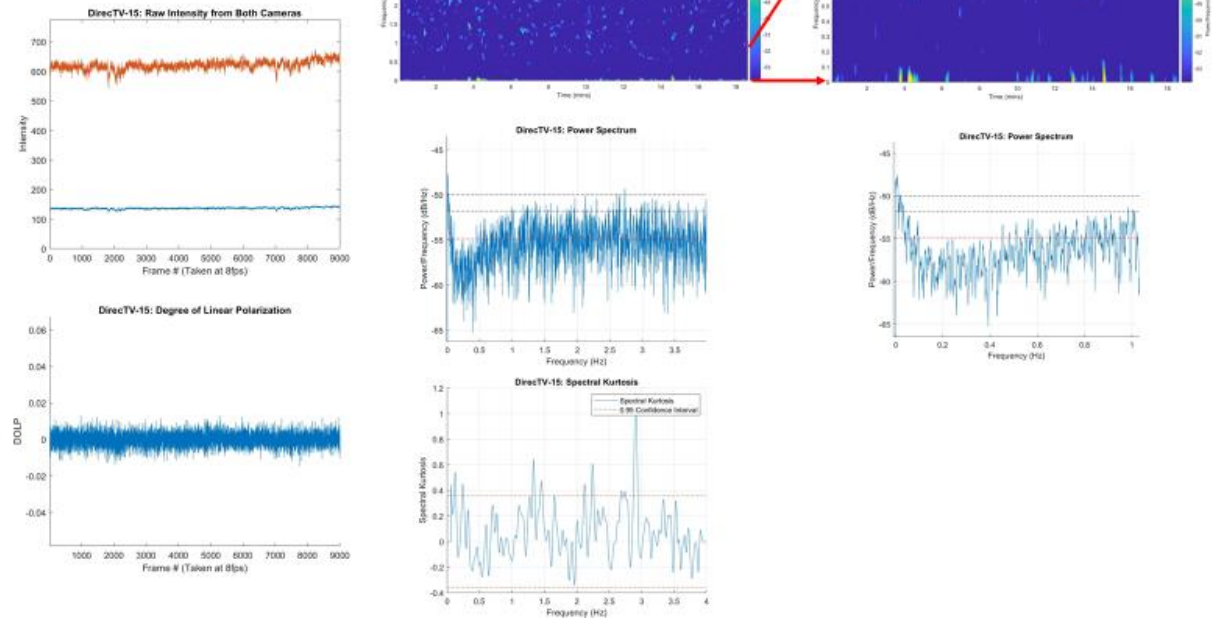
# 9/26/18 run1 part 4



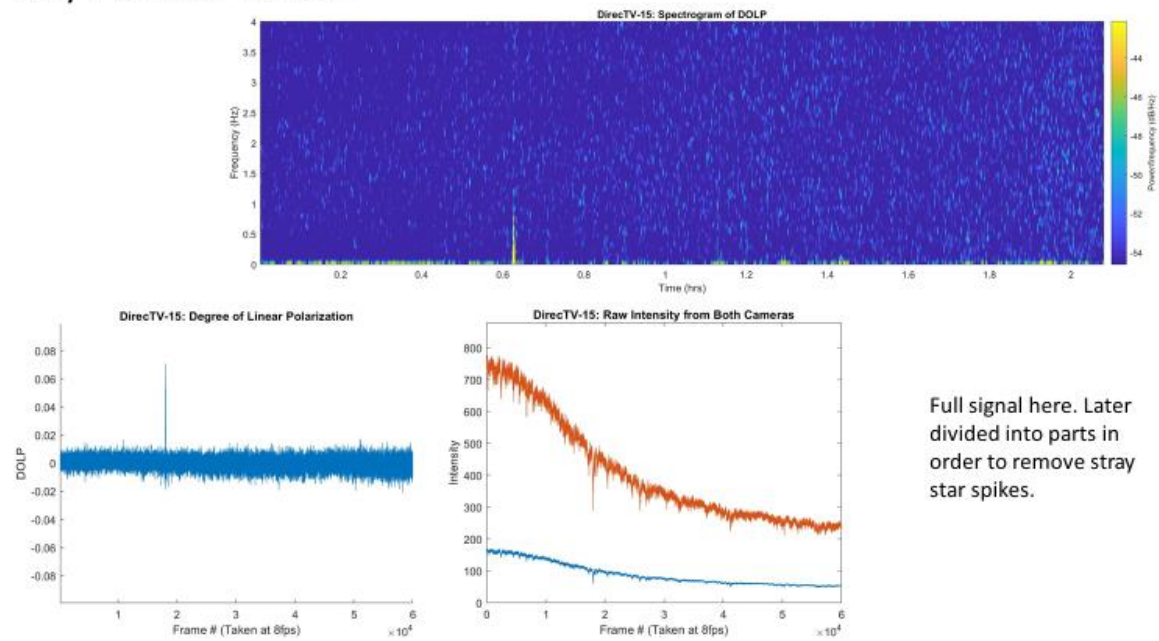
# 9/26/18 run2



## 10/20/18, Run1

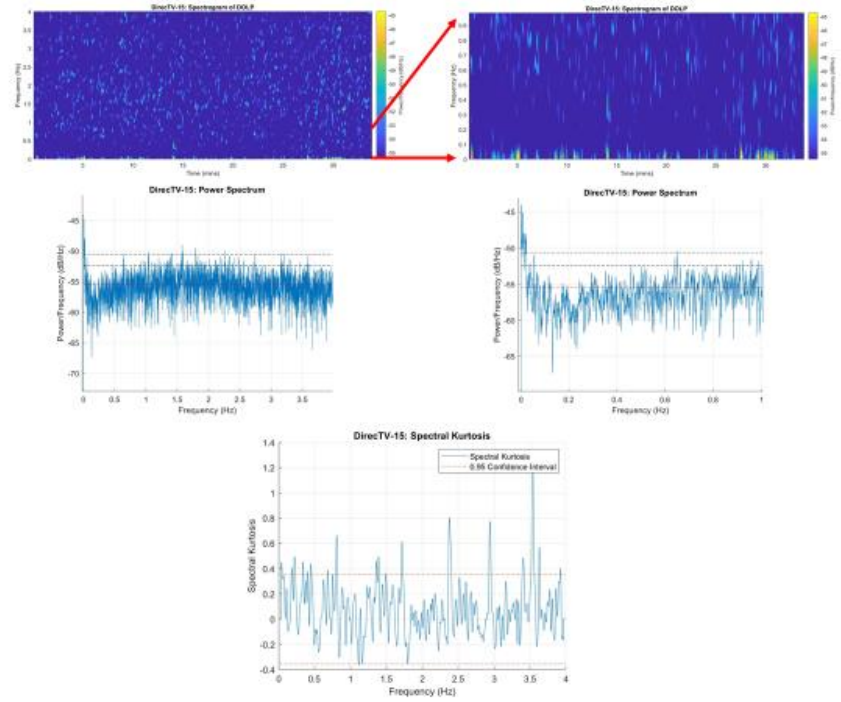
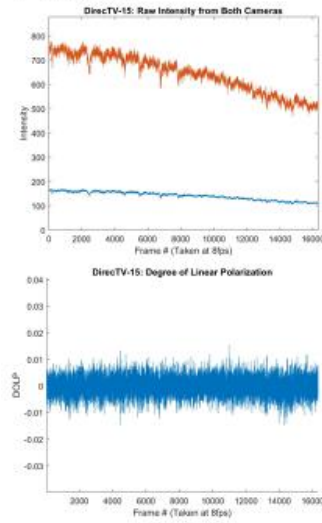


## 10/20/18 Run2

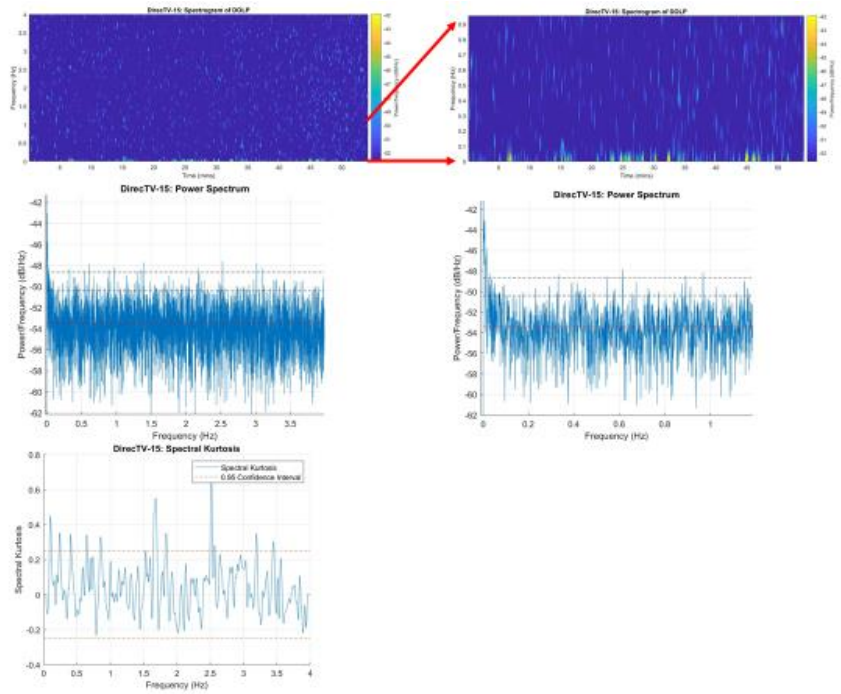
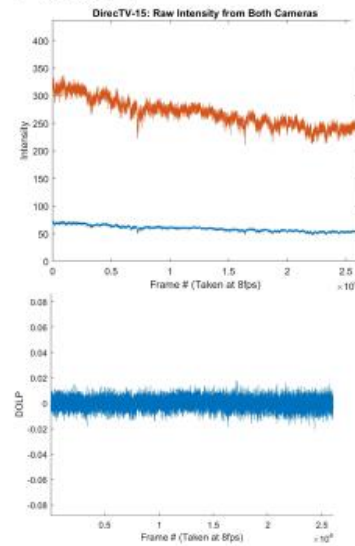


Full signal here. Later divided into parts in order to remove stray star spikes.

## 10/20/18, Run 2 Part 1



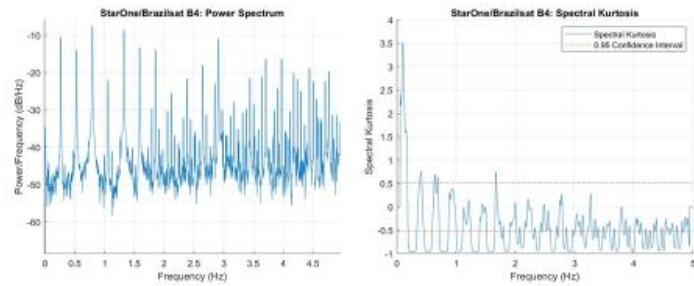
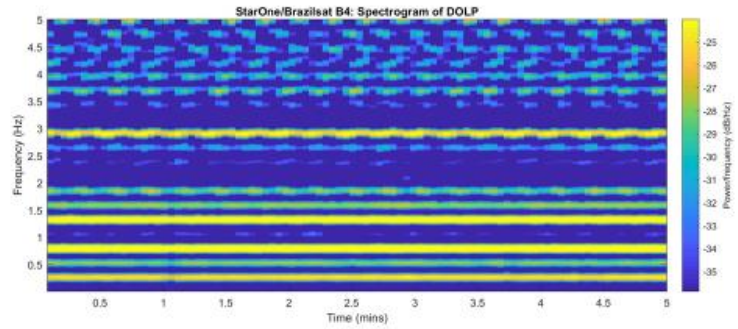
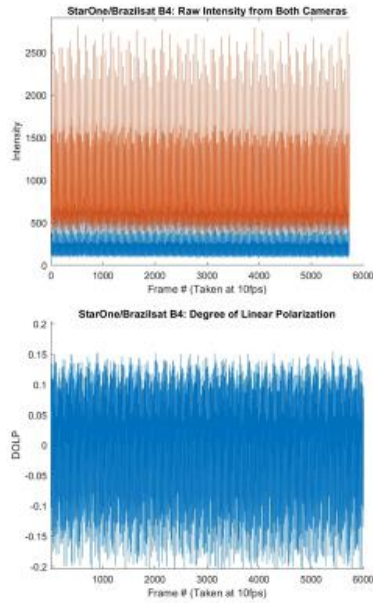
## 10/20/18, Run 2 Part 2



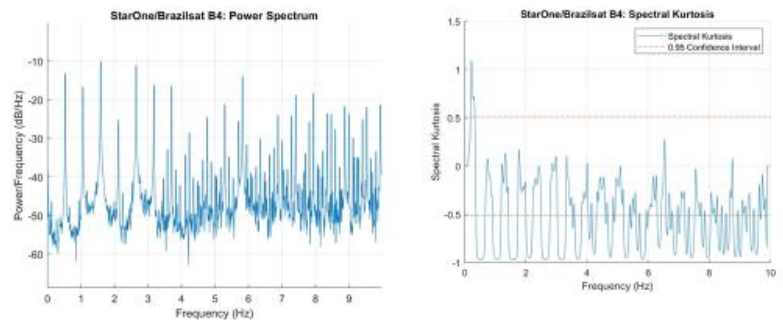
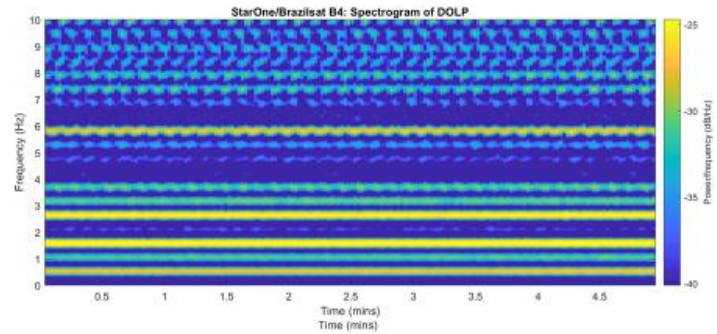
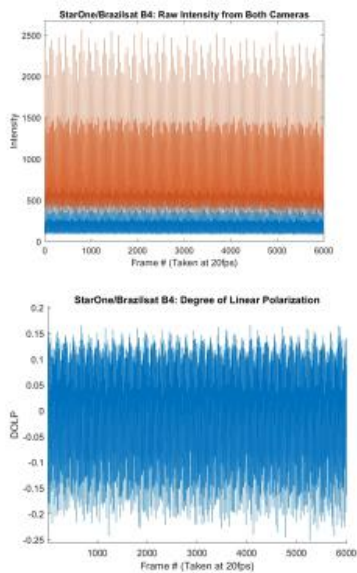


## StarOne/Brasilsat B4 – NORAD ID: 26446

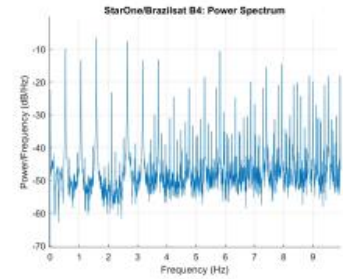
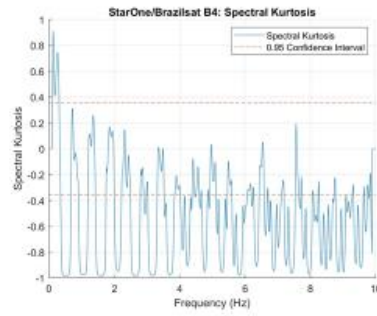
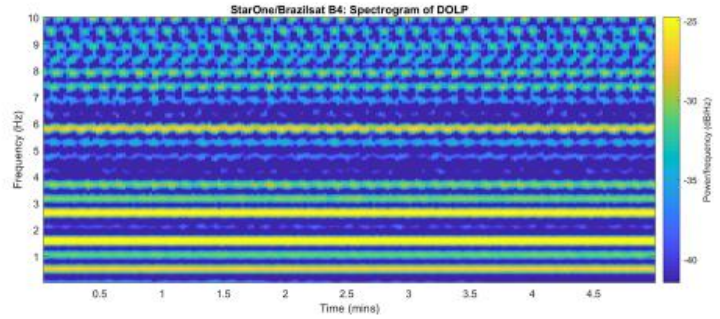
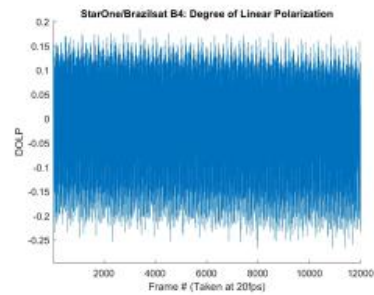
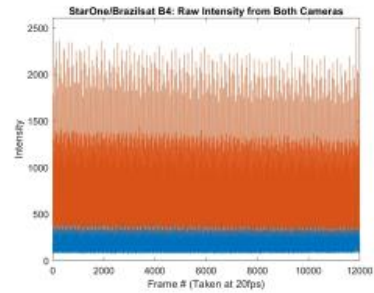
9/25/18 run 2



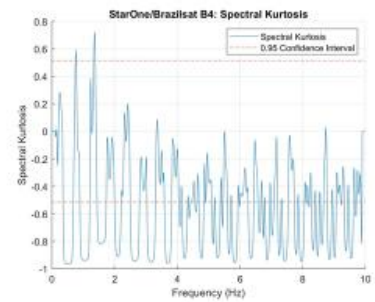
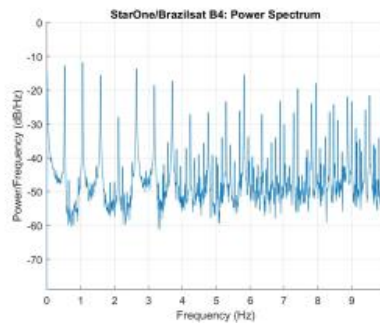
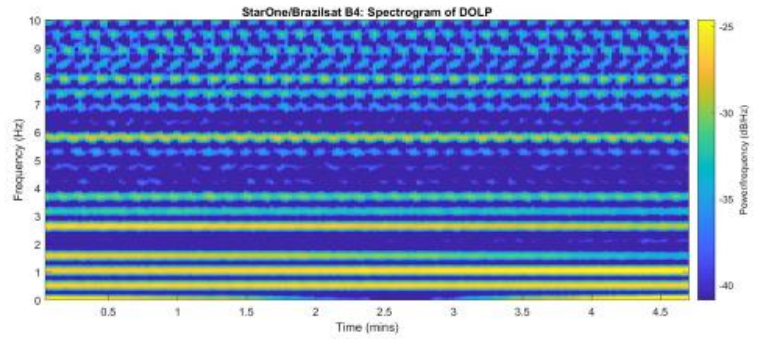
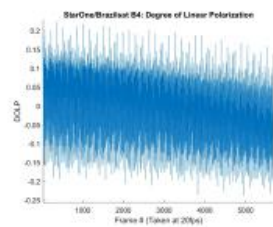
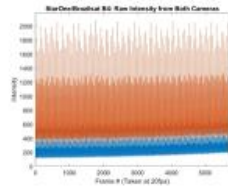
9/25/18 run3



9/25/18 run4

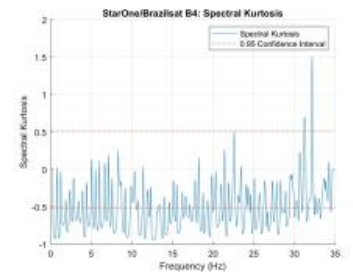
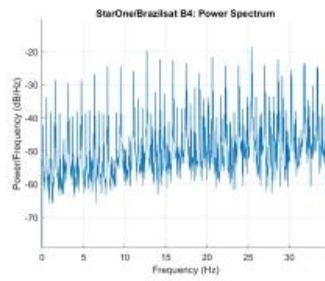
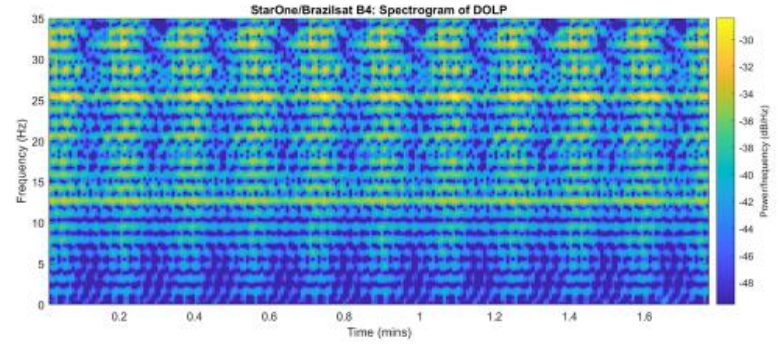
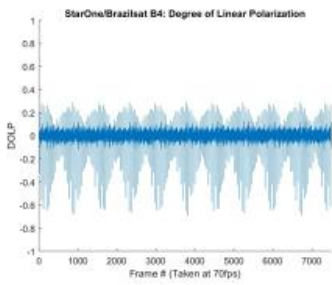
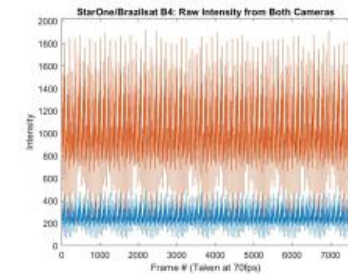


9/25/18 run5

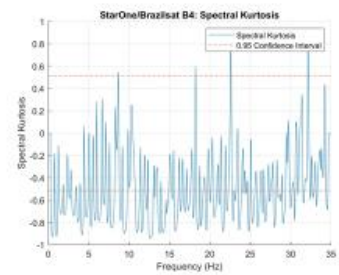
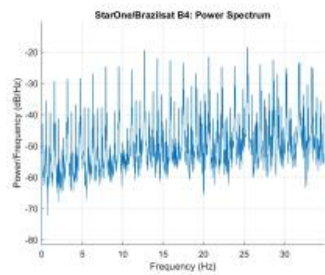
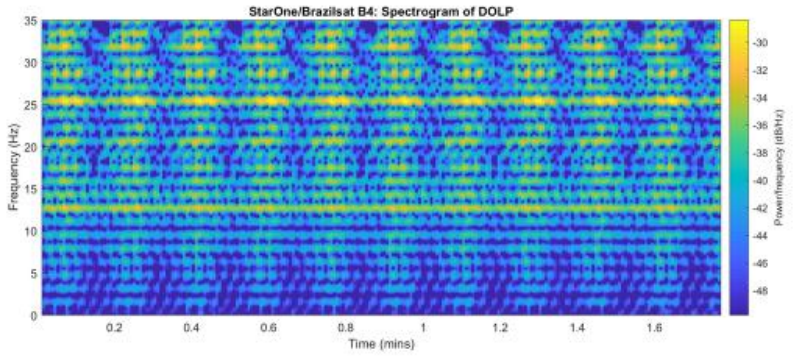
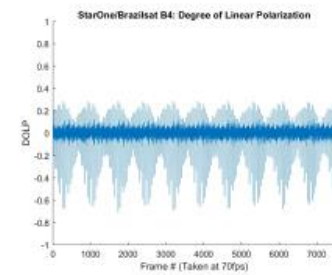
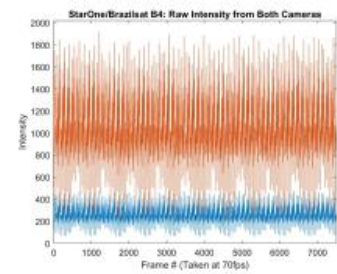




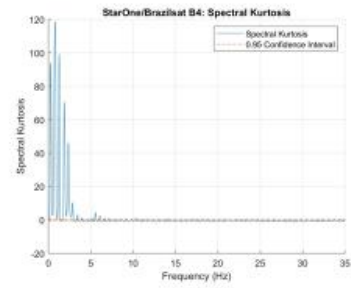
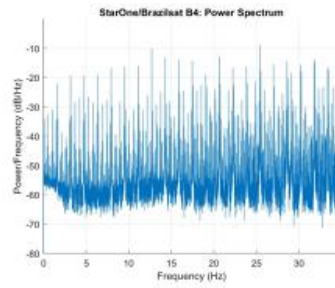
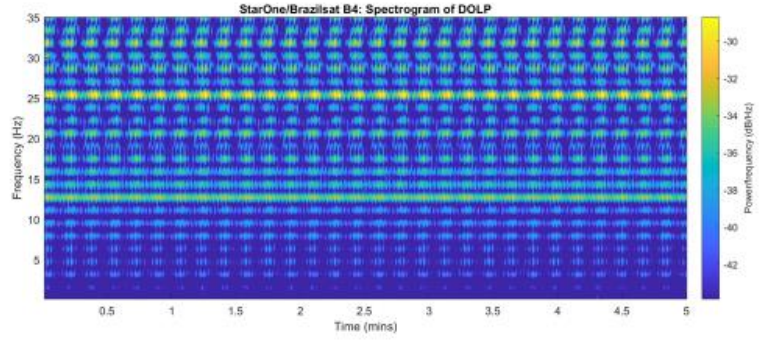
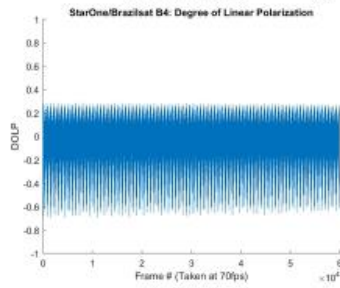
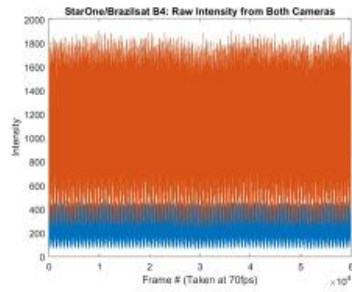
9/26/18 run2



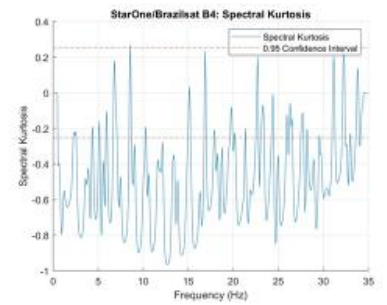
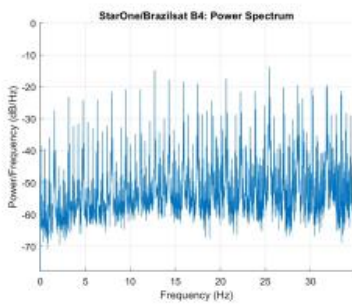
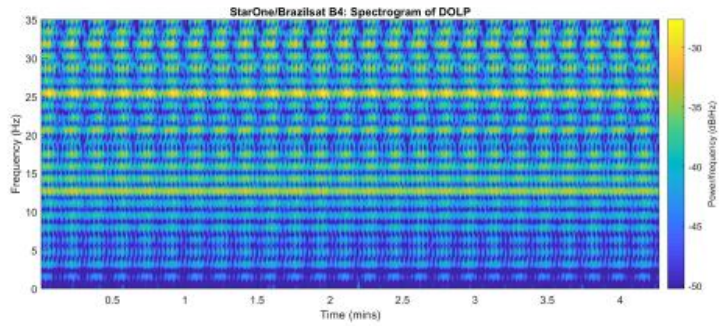
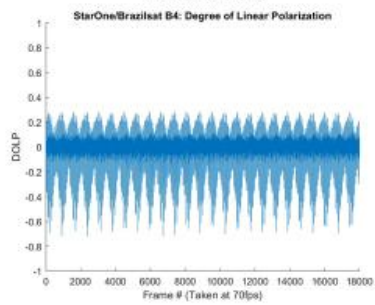
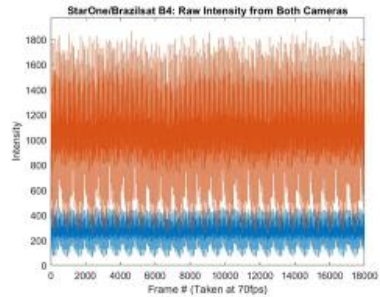
9/26 run3



9/26 run4

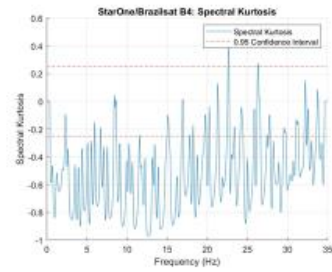
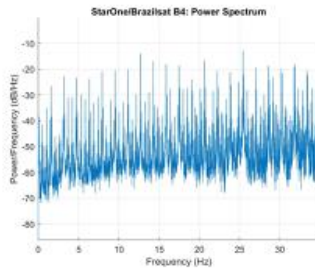
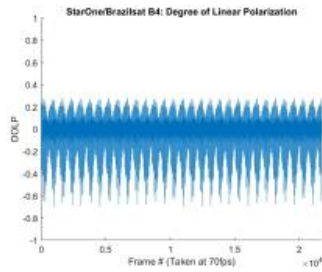
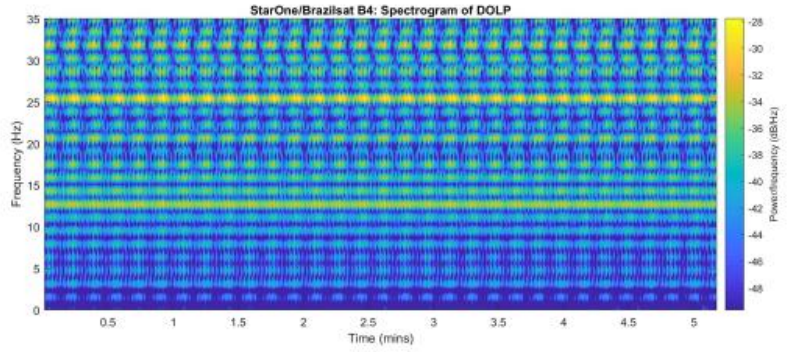
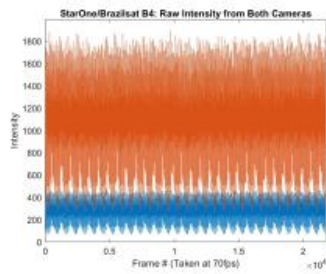


9/26 run5

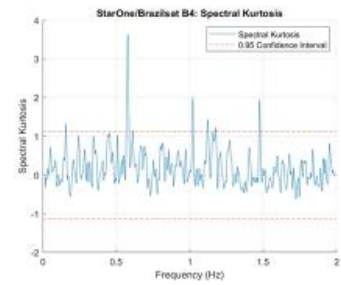
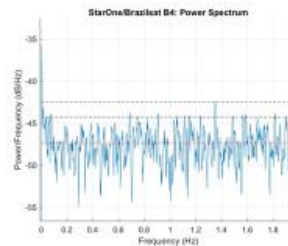
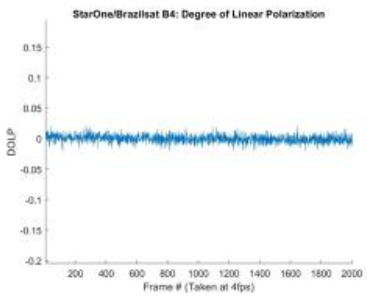
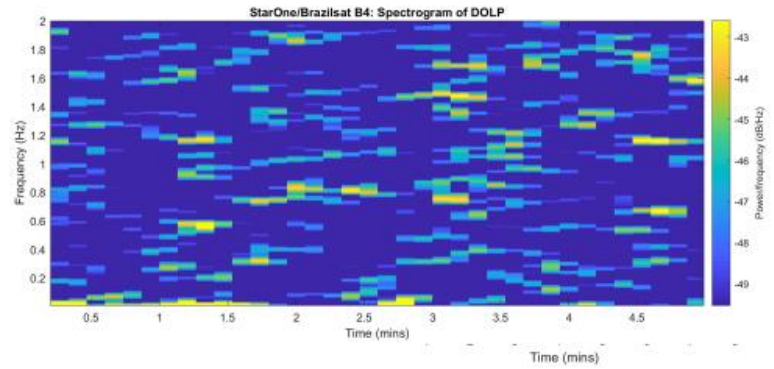
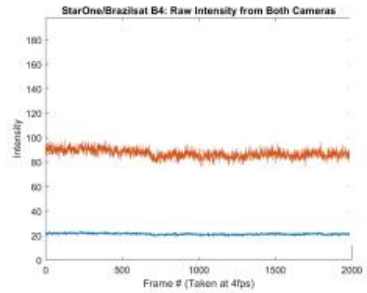




9/26 run6



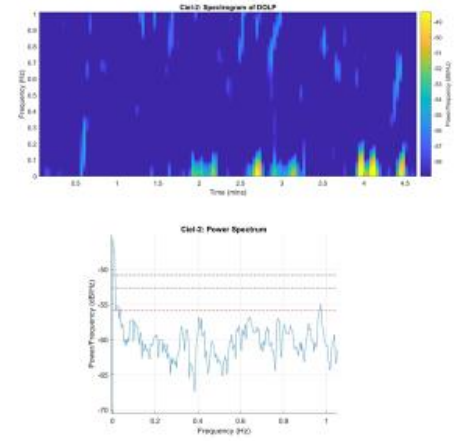
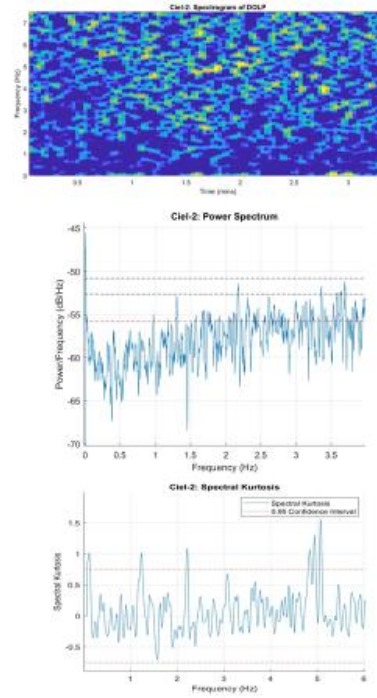
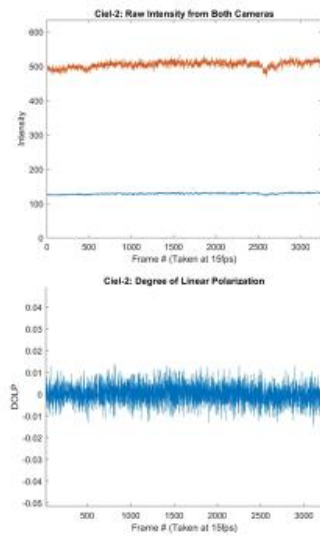
10/21/18



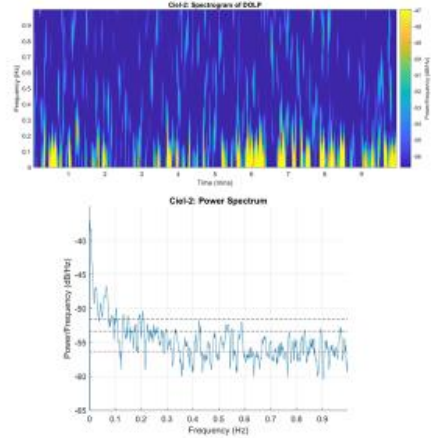
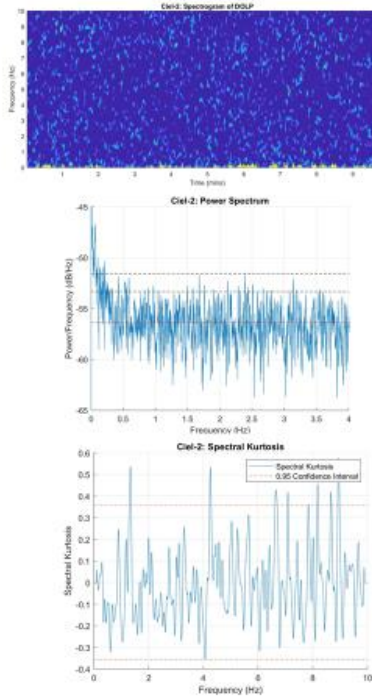
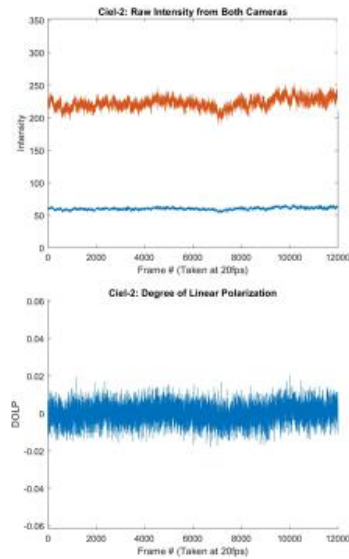


## Ciel-2 – NORAD ID: 33453

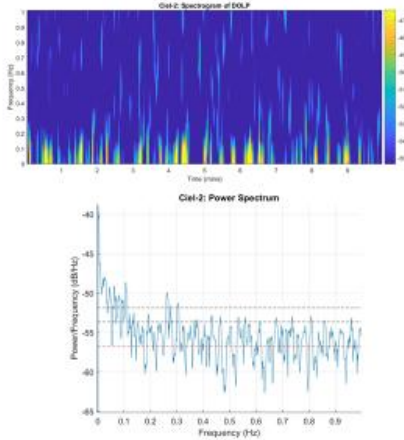
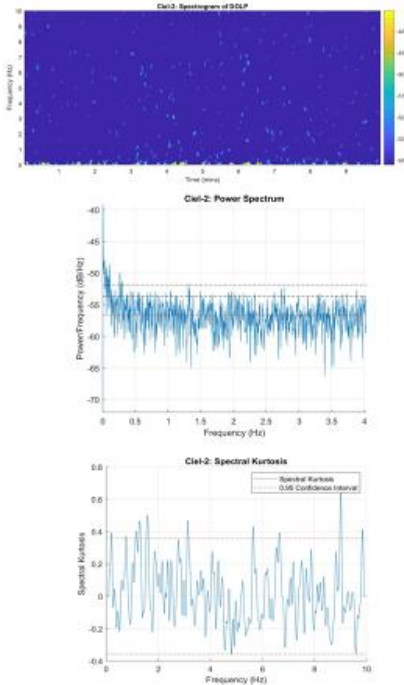
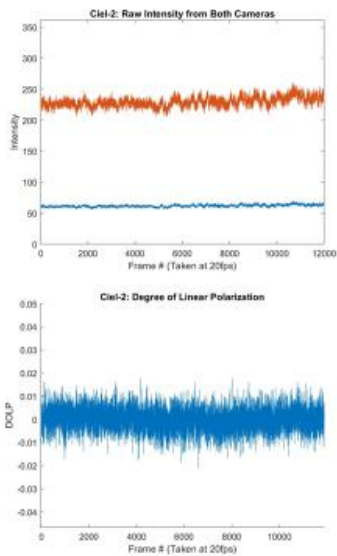
9/25/18, Run2



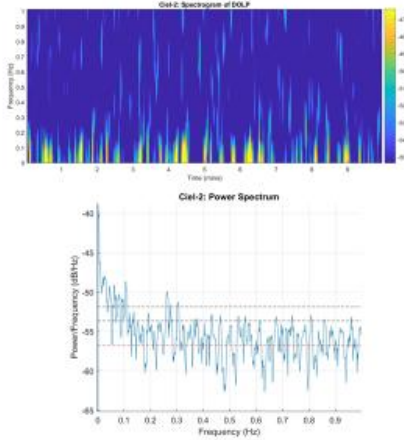
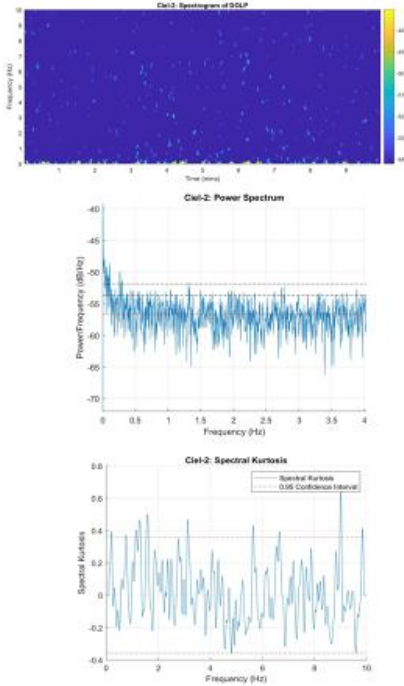
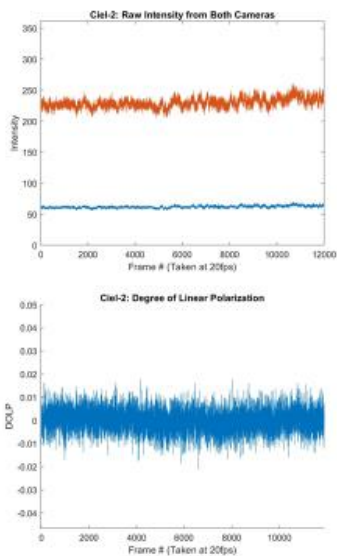
9/26/18, Run3



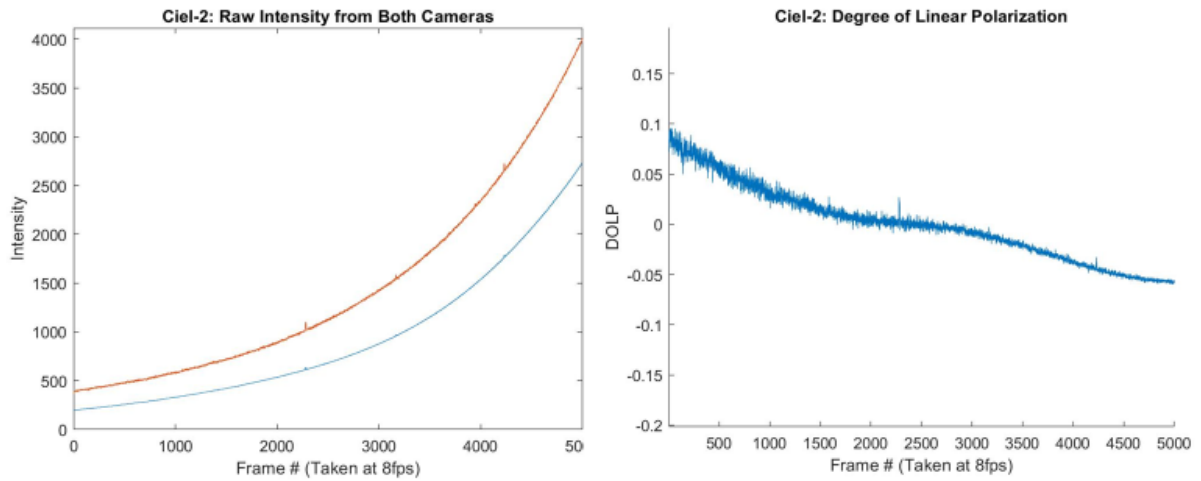
9/26/18, Run 4



9/26/18, Run 4

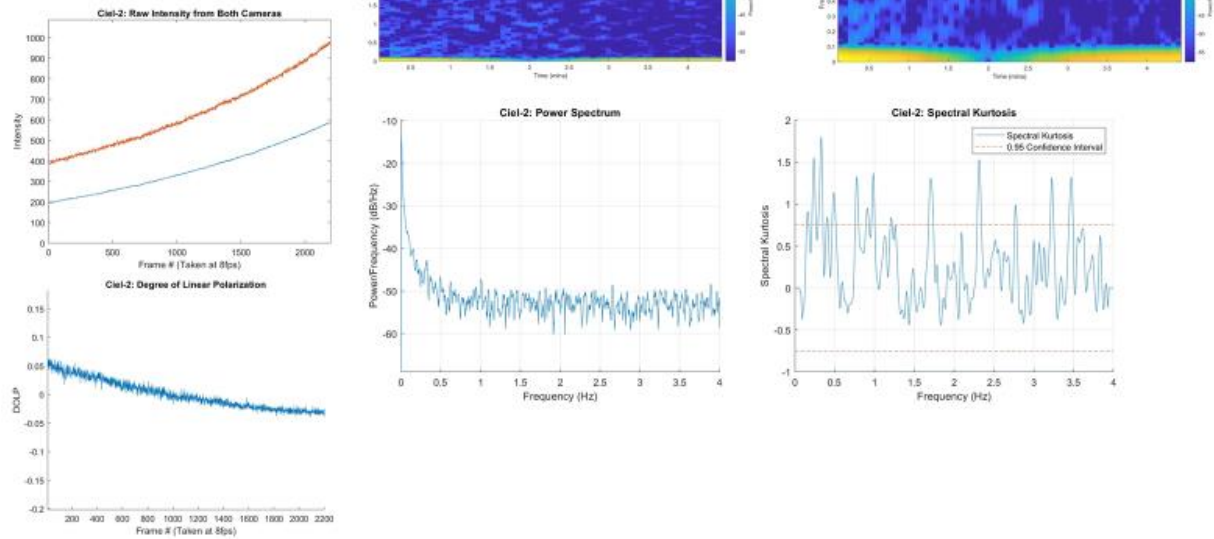


9/26/18, Run 9

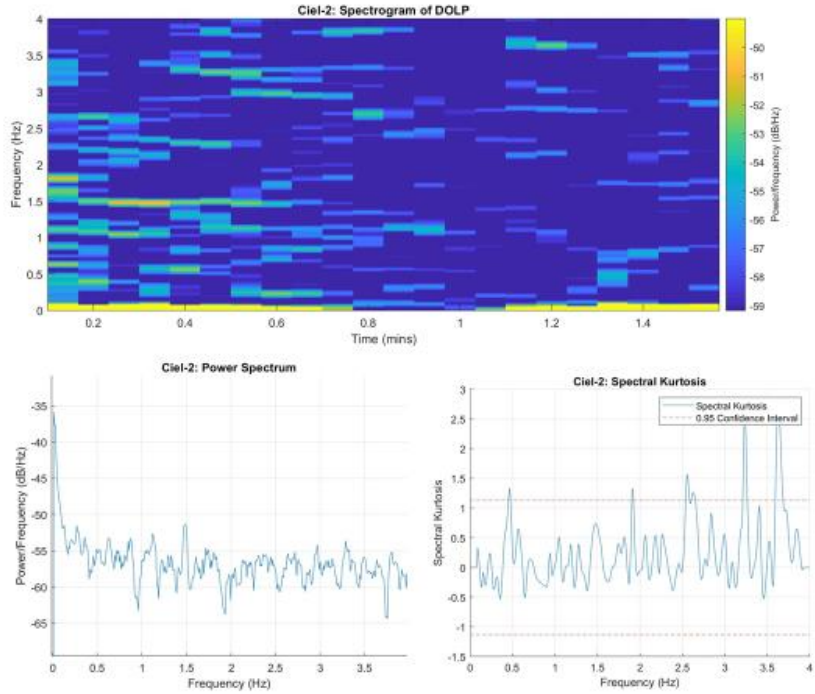
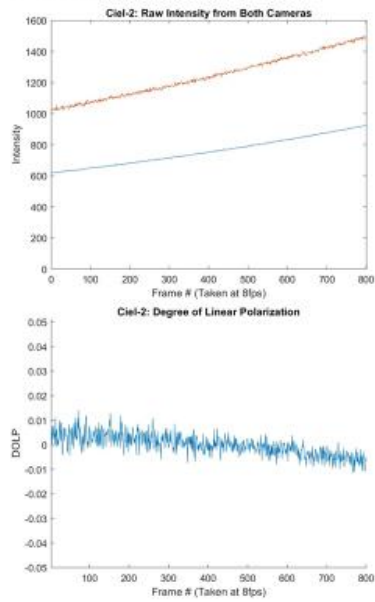


Full signal here. Later divided into parts in order to remove stray star spikes.

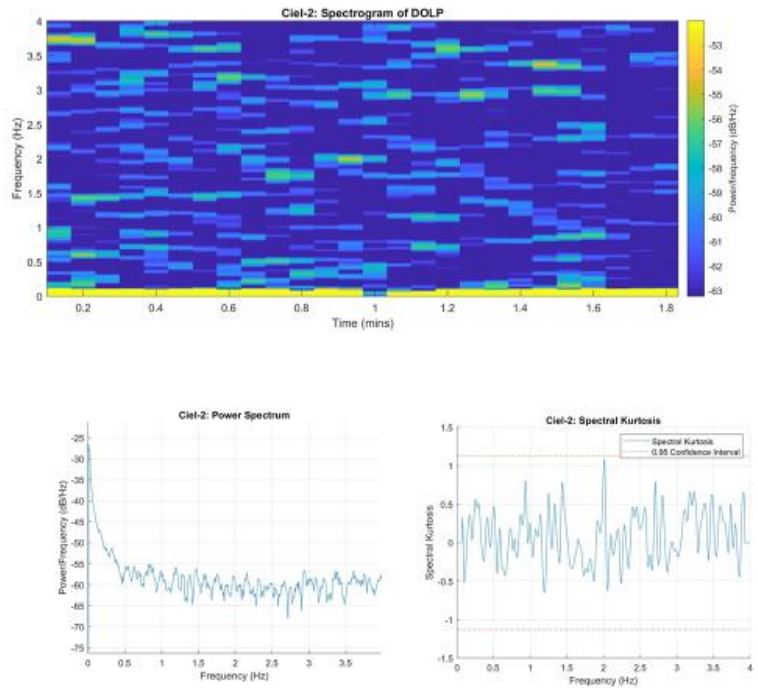
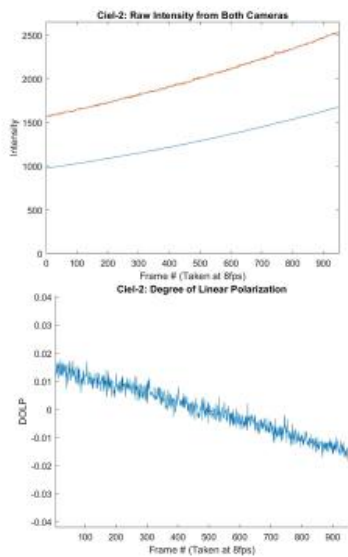
9/26/18, Run 9  
Part 1



## 9/26/18, Run 9 Part 2

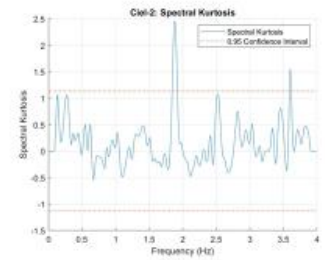
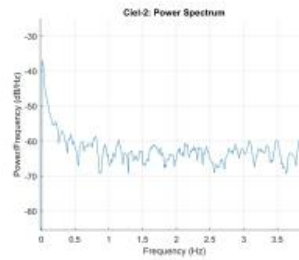
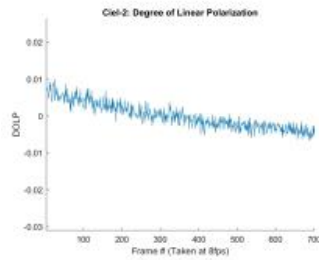
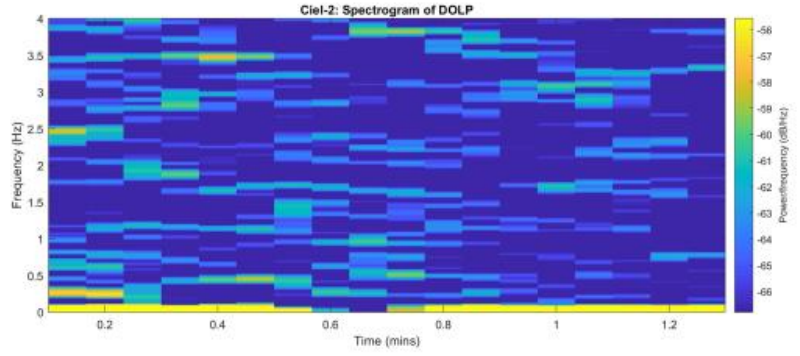
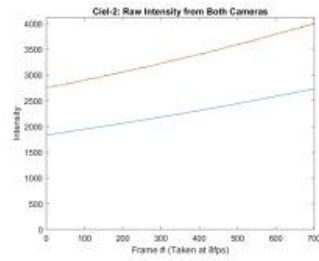


## 9/26/18, Run 9 Part 3

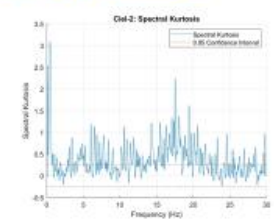
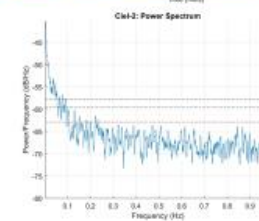
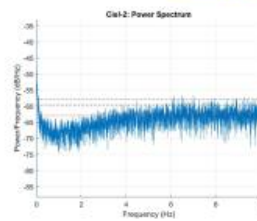
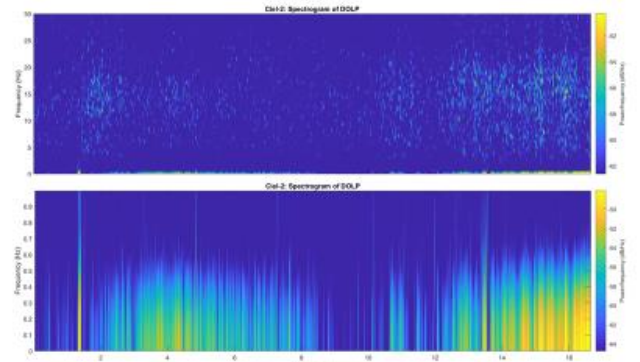
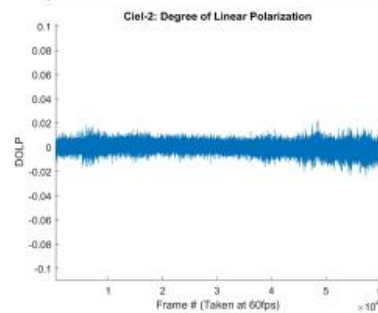
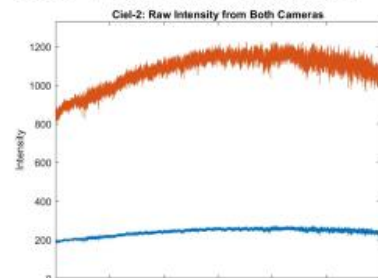




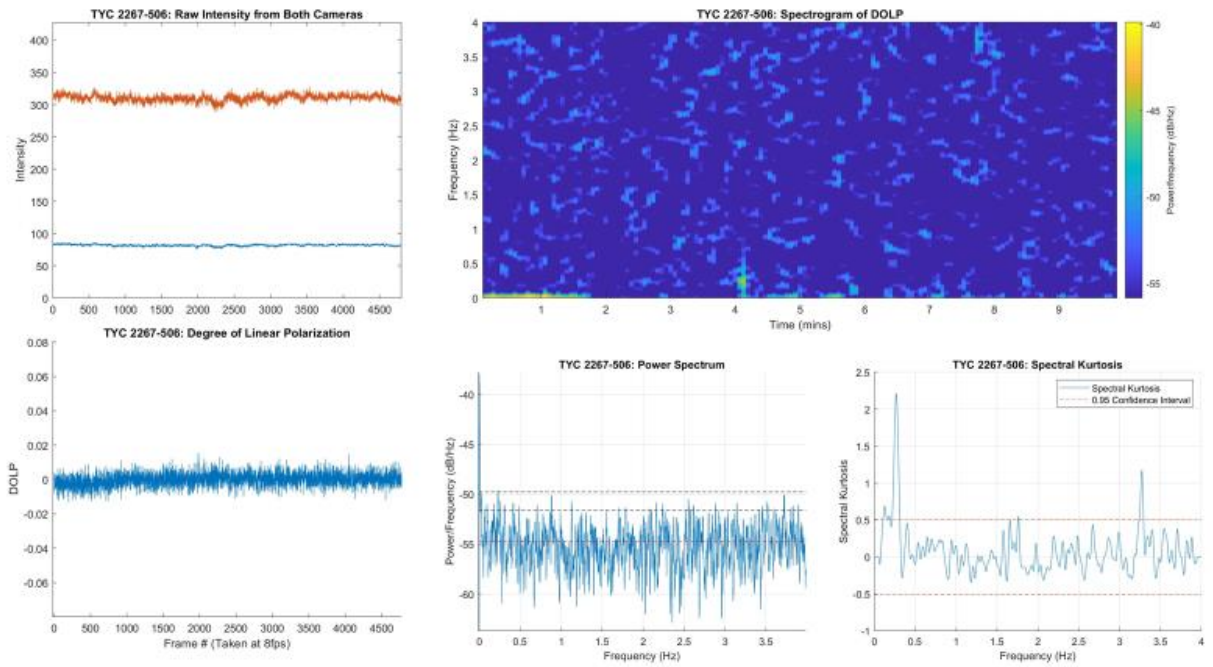
## 9/26/18, Run 9 Part 4



## 10/20/18 Run1



## Star TYC 2267-506 (September 26)



## 6.2 MATLAB code package definitions

Definitions of various functions used, as given by the official MATLAB help documentation [12].

### Periodogram()

Periodogram power spectral density estimate.

### Description

`pxx = periodogram(x)` returns the periodogram power spectral density (PSD) estimate, `pxx`, of the input signal, `x`, found using a rectangular window. When `x` is a vector, it is treated as a single channel. When `x` is a matrix, the PSD is computed independently for each column and stored in the corresponding column of `pxx`. If `x` is real-valued, `pxx` is a one-sided PSD estimate. If `x` is complex-valued, `pxx` is a two-sided PSD estimate. The number of points, `nfft`, in the discrete Fourier transform (DFT) is the maximum of 256 or the next power of two greater than the signal length.

`pxx = periodogram(x,window)` returns the modified periodogram PSD estimate using the window, `window`. `window` is a vector the same length as `x`.

`pxx = periodogram(x,window,nfft)` uses `nfft` points in the discrete Fourier transform (DFT). If `nfft` is greater than the signal length, `x` is zero-padded to length `nfft`. If `nfft` is less than the signal length, the signal is wrapped modulo `nfft` and summed using `datawrap`. For example, the input signal `[1 2 3 4 5 6 7 8]` with `nfft` equal to 4 results in the periodogram of `sum([1 5; 2 6; 3 7; 4 8],2)`.

`[pxx,w] = periodogram(__)` returns the normalized frequency vector, `w`. If `pxx` is a one-sided periodogram, `w` spans the interval  $[0,\pi]$  if `nfft` is even and  $[0,\pi)$  if `nfft` is odd. If `pxx` is a two-sided periodogram, `w` spans the interval  $[0,2\pi)$ .

`[pxx,f] = periodogram(__,fs)` returns a frequency vector, `f`, in cycles per unit time. The sample rate, `fs`, is the number of samples per unit time. If the unit of time is seconds, then `f` is in cycles/second (Hz). For real-valued signals, `f` spans the interval  $[0,fs/2]$  when `nfft` is even and  $[0,fs/2)$  when `nfft` is odd. For complex-valued signals, `f` spans the interval  $[0,fs)$ . `fs` must be the fourth input to `periodogram`. To input a sample rate and still use the default values of the preceding optional arguments, specify these arguments as empty, `[]`.

`[pxx,w] = periodogram(x,window,w)` returns the two-sided periodogram estimates at the normalized frequencies specified in the vector, `w`. `w` must contain at least two elements.

`[pxx, f] = periodogram(x, window, f, fs)` returns the two-sided periodogram estimates at the frequencies specified in the vector, `f`. `f` must contain at least two elements. The frequencies in `f` are in cycles per unit time. The sample rate, `fs`, is the number of samples per unit time. If the unit of time is seconds, then `f` is in cycles/second (Hz).

`[__] = periodogram(x, window, __, freqrange)` returns the periodogram over the frequency range specified by `freqrange`. Valid options for `freqrange` are: 'onesided', 'twosided', or 'centered'.

`[__] = periodogram(x, window, __, spectrumtype)` returns the PSD estimate if `spectrumtype` is specified as 'psd' and returns the power spectrum if `spectrumtype` is specified as 'power'.

`[__, pxxc] = periodogram(__, 'ConfidenceLevel', probability)` returns the `probability × 100%` confidence intervals for the PSD estimate in `pxxc`.

`[rpxx, f] = periodogram(__, 'reassigned')` reassigns each PSD estimate to the frequency closest to its center of energy. `rpxx` contains the sum of the estimates reassigned to each element of `f`.

`[rpxx, f, pxx, fc] = periodogram(__, 'reassigned')` also returns the nonreassigned PSD estimates, `pxx`, and the center-of-energy frequencies, `fc`. If you use the 'reassigned' flag, then you cannot specify a `probability` confidence interval.

`periodogram(__)` with no output arguments plots the periodogram PSD estimate in dB per unit frequency in the current figure window.



## Spectrogram()

Spectrogram using short-time Fourier transform

### Description

`s = spectrogram(x)` returns the short-time Fourier transform of the input signal, `x`. Each column of `s` contains an estimate of the short-term, time-localized frequency content of `x`.

`s = spectrogram(x,window)` uses `window` to divide the signal into segments and perform windowing.

`s = spectrogram(x,window,noverlap)` uses `noverlap` samples of overlap between adjoining segments.

`s = spectrogram(x,window,noverlap,nfft)` uses `nfft` sampling points to calculate the discrete Fourier transform.

`[s,w,t] = spectrogram(__)` returns a vector of normalized frequencies, `w`, and a vector of time instants, `t`, at which the spectrogram is computed. This syntax can include any combination of input arguments from previous syntaxes.

`[s,f,t] = spectrogram(__,fs)` returns a vector of cyclical frequencies, `f`, expressed in terms of the sample rate, `fs`. `fs` must be the fifth input to `spectrogram`. To input a sample rate and still use the default values of the preceding optional arguments, specify these arguments as empty, `[]`.

`[s,w,t] = spectrogram(x,window,noverlap,w)` returns the spectrogram at the normalized frequencies specified in `w`.

`[s,f,t] = spectrogram(x,window,noverlap,f,fs)` returns the spectrogram at the cyclical frequencies specified in `f`.

`[__,ps] = spectrogram(__)` also returns a matrix, `ps`, containing an estimate of the power spectral density (PSD) or the power spectrum of each segment.

`[__] = spectrogram(__,'reassigned')` reassigns each PSD or power spectrum estimate to the location of its center of energy. If your signal contains well-localized temporal or spectral components, then this option generates a sharper spectrogram.

`[__,ps,fc,tc] = spectrogram(__)` also returns two matrices, `fc` and `tc`, containing the frequency and time of the center of energy of each PSD or power spectrum estimate.

`[__] = spectrogram(__,freqrange)` returns the PSD or power spectrum estimate over the frequency range specified by `freqrange`. Valid options for `freqrange` are 'onesided', 'twosided', and 'centered'.

[\_\_] = spectrogram(\_\_, [spectrumtype](#)) returns PSD estimates if spectrumtype is specified as 'psd' and returns power spectrum estimates if spectrumtype is specified as 'power'.

[\_\_] = spectrogram(\_\_, 'MinThreshold', [thresh](#)) sets to zero those elements of [ps](#) such that  $10 \log_{10}(ps) \leq \text{thresh}$ . Specify thresh in decibels.

spectrogram(\_\_) with no output arguments plots the spectrogram in the current figure window.

spectrogram(\_\_, [freqloc](#)) specifies the axis on which to plot the frequency.

## kurtosis()

Kurtosis.

### Description

`k = kurtosis(X)` returns the sample kurtosis of `X`. For vectors, `kurtosis(x)` is the kurtosis of the elements in the vector `x`. For matrices `kurtosis(X)` returns the sample kurtosis for each column of `X`. For N-dimensional arrays, `kurtosis` operates along the first nonsingleton dimension of `X`.

`k = kurtosis(X, flag)` specifies whether to correct for bias (`flag` is 0) or not (`flag` is 1, the default). When `X` represents a sample from a population, the kurtosis of `X` is biased, that is, it will tend to differ from the population kurtosis by a systematic amount that depends on the size of the sample. You can set `flag` to 0 to correct for this systematic bias.

`k = kurtosis(X, flag, dim)` takes the kurtosis along dimension `dim` of `X`.

`kurtosis` treats NaNs as missing values and removes them.

### Spectral Kurtosis

Spectral kurtosis (SK) is a statistical tool that can indicate and pinpoint nonstationary or non-Gaussian behavior in the frequency domain, by taking:

- Small values at frequencies where stationary Gaussian noise only is present
- High positive values at frequencies where transients occur

This capability makes SK a powerful tool for detecting and extracting signals associated with faults in rotating mechanical systems. On its own, SK can identify features or conditional indicators for fault detection and classification. As preprocessing for other tools such as envelope analysis, SK can supply key inputs such as optimal band [13], [14].

The spectral kurtosis, or  $K(f)$ , of a signal  $x(t)$  can be computed based on the short-time Fourier transform (STFT) of the signal,  $S(t, f)$ :

$$S(t, f) = \int x(t) w(t - \tau) e^{-2\pi f \tau} d\tau,$$

where  $w(t)$  is the window function used in STFT.  $K(f)$  is calculated as:

$$K(f) = \frac{\langle |S(t, f)|^4 \rangle}{\langle |S(t, f)|^2 \rangle^2} - 2$$

where  $\langle \cdot \rangle$  is the time-average operator.

If the signal  $x(t)$  contains only stationary Gaussian noise, then  $K(f)$  at each frequency  $f$  has an asymptotic normal distribution with 0 mean and variance  $4/M$ , where  $M$  is the

number of elements along the time axis in  $S(t,f)$ . Hence, a statistical threshold  $s_\alpha$  given a confidence level  $\alpha$  is:

$$s_\alpha = \Phi^{-1}(\alpha) \frac{2}{\sqrt{M}}$$

where  $\Phi^{-1}$  is the quantile function of the standard normal distribution.

It is important to note that the STFT window length  $N_w$  directly drives frequency resolution, which is  $f_s/N_w$ , where  $f_s$  is the sample frequency. The window size must be shorter than the spacing between transient impulses, but longer than the individual transient impulses.

## 7 References

- [1] Antoni, J. "The Spectral Kurtosis: A Useful Tool for Characterising Non-Stationary Signals." *Mechanical Systems and Signal Processing*. Vol. 20, Issue 2, 2006, pp. 282–307.
- [2] Antoni, J., and R. B. Randall. "The Spectral Kurtosis: Application to the Vibratory Surveillance and Diagnostics of Rotating Machines." *Mechanical Systems and Signal Processing* . Vol. 20, Issue 2, 2006, pp. 308–331.
- [3] Gibson, B. et al., Optical-Infrared colors of GEO Satellites, Proc. AMOS Tech. Conf. (2013)
- [4] Giles, A. B. & Hill, K. M., Optical observations of geostationary spin-stabilised satellites, *Astrophysics and Space Science* (ISSN 0004-640X), vol. 147, no. 2, Aug. 1988, p. 359-379.
- [5] Hart, M. et al., Resolved Observations of Geostationary Satellites from the 6.5 m MMT, Proc. AMOS Tech. Conf. (2015)
- [6] Hill, K. M., Giles, A. B., & Watson, R. D., Fast photometry of the Crab, SN 1987A and Aussat, *Astronomical Society of Australia, Proceedings* (ISSN 0066-9997), vol. 8, no. 1, 1989, p. 75-77.
- [7] Mohsenizadeh, Navid, Simulation Methodologies for Satellite Soar Array Dynamics, a Thesis submitted to the Office of Graduate Studies of Texas A&M University, (Aug. 2010)
- [8] Nader Sawalhi, Robert B. Randall ,THE APPLICATION OF SPECTRAL KURTOSIS TO BEARING DIAGNOSTICS, Proceedings of ACOUSTICS 2004, 3-5 November 2004, Gold Coast, Australia.
- [9] Slater, D., Passive long range acousto-optic sensor, Free-Space Laser Communications VI, (Proc. SPIE) 6304 (2006)
- [10] Valeriu Vrabie, Pierre Granjon, Christine Serviere. Spectral kurtosis: from definition to application. 6th IEEE International Workshop on Nonlinear Signal and Image Processing (NSIP 2003), 2003, Grado-Trieste, Italy. 2003. <hal-00021302>
- [11] Watson, Z. et al., Remote Acoustic Imaging of Geosynchronous Satellites Proc. AMOS Tech. Conf. (2017)

### Websites:

- [12] <https://www.mathworks.com/help/matlab/>  
COPYRIGHT 1984–2018 by The MathWorks, Inc.
- [13] Andor Zyla 4.2+ sCMOS Detector Specifications: [http://www.andor.com/scientific-cameras/neo-and-zyla-scmos-cameras/zyla-42-plus-scmos?gclid=CjwKCAiA\\_ojVBRAIeiwAOLRxI9te26EemAVa65FNXmv\\_F5Dbzmy-EszDQTIUKzlbzo2Fqvvg2Qj\\_6hoC6HgQAvD\\_BwE#specifications](http://www.andor.com/scientific-cameras/neo-and-zyla-scmos-cameras/zyla-42-plus-scmos?gclid=CjwKCAiA_ojVBRAIeiwAOLRxI9te26EemAVa65FNXmv_F5Dbzmy-EszDQTIUKzlbzo2Fqvvg2Qj_6hoC6HgQAvD_BwE#specifications)
- [14] Grasshopper Detector specifications: <https://www.ptgrey.com/grasshopper3-23-mp-mono-usb3-vision-sony-pregius-imx174-camera>
- [15] <https://www.boeing.com/history/products/601-satellite.page>
- [16] 61 Inch Kuiper Telescope webpage: <http://james.as.arizona.edu/~psmith/61inch>
- [17] 61" Kuiper Telescope Specifications, <https://www.as.arizona.edu/kuiper-61-telescope>
- [18] <https://www.airbus.com/space/telecommunications-satellites/eurostar-series.html#e3000>
- [19] <http://www.astronautix.com/s/spacebus4000.html>